WARWICK
THE UNIVERSITY OF WARWICK

Original citation:
Fukumoto, Kazui, Wang, Changjian and Wen, Jennifer X.. (2018) Large eddy simulation of upward flame spread on PMMA walls with a fully coupled fluid–solid approach. Combustion and Flame, 190 . pp. 365-387.

Permanent WRAP URL:
http://wrap.warwick.ac.uk/97109

A note on versions:
The version presented here may differ from the published version or, version of record, if you wish to cite this item you are advised to consult the publisher's version. Please see the 'permanent WRAP url' above for details on accessing the published version and note that access may require a subscription.

For more information, please contact the WRAP Team at: wrap@warwick.ac.uk

warwick.ac.uk/lib-publications

Large eddy simulation of upward flame spread on PMMA walls with a fully coupled fluid-solid approach

Kazui Fukumoto[a], Changjian Wang[b] and Jennifer Wen[a,1]

[a]Warwick FIRE, University of Warwick, Coventry CV4 7AL, United Kingdom Institution

[b]School of Civil Engineering, Hefei University of Technology, Hefei, 230009, Anhui, China

Abstract

A fully coupled fluid-solid approach has been developed within FireFOAM 2.2.x, a Large Eddy Simulation (LES) based fire simulation solver within the OpenFOAM® toolbox. Due consideration has been given to couple the radiative heat transfer and soot treatment with pyrolysis calculations. Combustion is modelled using the newly extended eddy dissipation concept (EDC) for the LES published by the authors' group. Soot formation and oxidation are handled by the published extension of the laminar smoke point concept to turbulent fires using the partially stirred reactor (PaSR) concept also from the authors' group. The gases radiation properties are evaluated using the established weighted sum of grey gas model while soot absorption coefficient is calculated using a single Planck-mean absorption coefficient. The effect of in-depth radiation is treated with the relatively simple Beer's law and the solid surface regression length is calculated from the local pyrolysis rate. Systematic validation studies have been conducted with several published experiments including simple pyrolysis test without the gaseous region, small scale wall fires and large scale flame spread. The predictions are in very good agreement with the relevant experimental data, demonstrating that the present modelling approach can be used to predict upward flame spread over PMMA with reasonable accuracy. Further parametric studies have also been conducted to demonstrate the effectiveness of the present modifications to capture the underlying physics. The detailed field predictions for vortex structures and flame volume including laminar-turbulent transition have also been analysed to uncover further insight of the unsteady flame spread phenomena. Potentially, the model can be used to aid further fundamental studies of the flame spread

---

[1] *Corresponding author email: Jennifer.Wen@warwick.ac.uk*

phenomena such as investigating the effects of width, inclination angles and side walls on flame spread as well as the predictions of flame spread in practical applications.

Keywords

Upward flame spread, Fully coupled fluid-solid approach, Large eddy simulation, PMMA

1. Introduction

Upward flame spread on a combustible fuel surface is of considerable importance to fire safety, partially because its spread rate is much faster than that over horizontal or inclined fuel surface [1]. Considerable efforts have been devoted to experimental studies of this phenomenon and some numerical studies have also been reported. Polymethyl methacrylate (PMMA) is frequently used in these investigations partially because its physical properties are well known [2,3].

Orloff et al. [4] and Quintiere et al. [5] reported important findings from their experiments about the change of spread rate with time, the relative contribution of radiative and convective heat transfer as well as heat flux distributions. Saito et al. [6] investigated upward spread of flames along thermally thick PMMA and reported detailed measurements of spread rates, flame heights and surface temperatures. More recently, Leventon and Stoliarov [7] measured the heat flux on the surface of a relatively small PMMA sample during upward flame spread. Pizzo et al. [8] experimentally investigated transient pyrolysis of thick clear PMMA slabs exposed to radiant heat fluxes of 14 and 18 kW/m^2. They also conducted a second series of experiments in which the PMMA samples were exposed to incident flame heat flux of 24.5 kW/m^2. Singh and Gollner [9] measured the average mass-loss rates and local temperature profiles in the boundary-layer diffusion flame established over a PMMA surface. They also developed a novel methodology to determine the various components of flame heat flux in the pyrolysis and plume regions. Liang et al. [10] experimentally investigated vertical upward flame spread over PMMA and reported measurements of flame heights, flame heat flux to the fuel surface and flame spread rate.

A number of investigators have focused on the solid phase pyrolysis and combustion. Fernandez-Pello [2] developed a theoretical model for upward laminar flame spread, which became the basis for the various pyrolysis models subsequently developed. Chaos et al. [3] optimized the pyrolysis model parameters of various materials using evolutionary optimization methodologies and validated the predictions with in-house experimental data. Pizzo et al. [8] developed a one dimensional pyrolysis model and simulated the solid phase combustion for validation. They found that the surface regression length due to the high incident heat flux and wall temperature was almost compensated by the re-radiation and gasification heat under the flaming condition. Leventon et al. [11] developed a PMMA pyrolysis model based on their previous measurements. Their predictions of the vertical burning and flame spread on a small PMMA sample achieved reasonably good agreement with the measurements. Kacem et al. [12] carried out comparative evaluation of clear PMMA pyrolysis models and found that the pyrolysis model with in-depth radiation improved the simulation results. Gong et al. [13] investigated the effect of PMMA sample width on downward flame spread, and suggested a semi-empirical model to estimate the leading edge angle, mass loss rate and flame spread.

Relatively few studies have been conducted in the computational fluid dynamics (CFD) context to incorporate the three dimensional (3-D) geometrical effects as well as the effects of the pilot burners. Consalvi et al. [14] conducted a 2-D simulation with the Reynolds Averaged Navier Stokes (RANS) approach and found that the contribution to heating process in the region of intermittent and continuous flames was important whereas less critical for the plume region. Kwon et al. [15] performed Large Eddy Simulation (LES) of a 3-D case. While their predicted maximum heat release rate appeared to be reasonable but the predicted flame spread rate had relatively large discrepancies. Ren et al. [16] conducted LES of the vertical turbulent wall fire using FireFOAM [17], the LES based fire simulation solver within the OpenFOAM® toolbox [18]. Their predictions were in qualitative agreement with the experimental observations while the small discrepancy was attributed to the overestimation of the size of the laminar flame region near the wall. They subsequently [19]

3

investigated the correlation between the heat flux and first grid size from the wall and found that setting it to 3 mm led to grid independent results using the wall-adapting local eddy-viscosity (WALE) model to resolve the near wall dynamics. Although it is possible to use a wall model to avoid using fine resolutions, this would constitute an additional source of error because of modelling near wall dynamics [20]. Yuan et al. [21] performed LES of a polyurethane foam (PUF) compartment fire and investigated the effect of ventilation conditions. However, the investigations of Ren et al. [16,19] and Yuan et al. [21] did not include flame spread, the former focused on wall fires while the later on the combustion process inside the compartment.

Most other previous CFD studies of flame spread are based on 2-D [2,14,22]. The neglecting of the dynamics in the third direction would inevitably results in the omission of some physics, e.g. the effect of side walls. Liang et al's experiment [10] revealed that the pyrolysis front has a convex shape without side walls. Gong et al.'s [13] captured the convex shape but they only simulated the solid phase.

None of the previous studies captured the laminar-turbulence transition [14,15], which was experimentally observed by Orloff [4] at location 0.18 m from the bottom of the PMMA wall. The soot distribution is considered one of the important factors to the total heat flux in flame spread [14,23] but no validation has been carried out for the prediction of soot in the flame spread scenario. Furthermore, previous numerical flame spread studies [2,14,15] have only reported predictions of the total heat flux without distinguishing the relative contributions of convective, radiative, and re-radiative heat fluxes while such details will aid further insight of the underlying physics of the flame spread scenario.

The present study reports on the development and validation of a fully coupled fluid-solid approach for flame spread using 3-D geometry with some recent development in the combustion, soot and radiation treatment in fire simulations conducted by the authors' group [24–27]. Some modifications have been introduced to better capture the underlying physics during flame spread which involves laminar-turbulent transition from the base of the PMMA upwards and as the flame

moves away from the wall. A characteristic length that is more representative of the phenomena and the mean beam length for the associated flame radiation have been proposed. The existing pyrolysis model in FireFOAM has been modified to capture in-depth radiation within the PMMA sample and surface regression accompanying flame spread. Further investigations have also been carried out on the soot formation and oxidation during flame spread and its impact on the heat flux. The developments of the vortex structures and flame volume including laminar-turbulent transition have been analysed to gain insight of the unsteady flame spread phenomena.

Although during the earlier stage of the development, the authors presented some preliminary results at the US Combustion meeting in 2015 [28], the details of the methodology including further development after the conference presentation and final validations are reported for the first time in the present paper.

2   Numerical solver

The LES based FireFOAM solver is used as the basic numerical framework for the present study. For clarity, the governing equations in FireFOAM are given in Appendix A. As mentioned earlier, the code has previously been used to simulate wall fires by Ren et al. [19]. It uses a second order accurate central linear scheme for the momentum equations, the linear scheme limited by total variation diminishing (TVD) to the governing equations of the mass fraction of chemical species and the energy equation; and the second order backward differential scheme for time marching. The momentum and continuity equations are coupled by the Pressure Implicit with Splitting of Operator (PISO) algorithm [29] with outer iteration, which is referred as PIMPLE in OpenFOAM [18], and the number of the outer iteration is set to 2 in the present study. The turbulent Schmidt number Sc_t and the turbulent Prandtl number Pr_t were set to 0.85. The in-house version of FireFOAM which contains recent development within the authors' group [24–27] is used.

2.1 The modification of the extended EDC model

The extended EDC model [25,26] is described in Appendix B. In this section, only new modifications introduced by the present authors to facilitate flame spread study are described. The extended EDC model requires the integral length L' as input. The characteristic length for pool fires was used by Chen et al. [25,26]. However, during flame spread, the characteristic length should not change with the width of the PMMA. The heat release rate per width of the PMMA is hence used to calculate the Froude number [14], which is then used to calculate the characteristics length of the spreading flame as:

$$L' = \left(\frac{q'}{\rho_\infty Cp_\infty T_\infty g^{1/2}} \right)^{2/3} \quad \text{m,} \tag{1}$$

where q' is the heat release rate per width of the PMMA [W/m], ρ_∞ the ambient density, Cp_∞ the ambient specific heat at constant pressure, g the gravitational acceleration and T_∞ the ambient temperature. q' is calculated from the PMMA heat of combustion and mass loss rate, which is calculated from the pyrolysis model (independent of the EDC).

The WALE model [30] is used to obtain the SGS kinematic viscosity ν_{SGS} for sub-grid scale (SGS) turbulence with the model parameter C_w set to 0.55 following Ren et al. [19]. The reader is recommended to refer to Nicoud et al. [30] for details of the model. The SGS turbulent kinetic energy k_{SGS} is not calculated in the WALE model but required for the extended EDC model in Eq. (57) in Appendix B. It is calculated from ν_{SGS} following Colin et al. [31]:

$$k_{SGS} = \frac{1}{2} |\mathbf{u_{SGS}}|^2 \quad \text{m}^2/\text{s}^2\text{, and} \tag{2}$$

$$|\mathbf{u_{SGS}}| = \frac{\nu_{SGS}}{C_s \Delta_{filter}} \quad \text{m/s,} \tag{3}$$

where $\mathbf{u_{SGS}}$ is the SGS velocity vector, C_s the Smagorinsky constant and Δ_{filter} the filter width. Nicoud et al. [30] suggested that $0.55 \leq C_w \leq 0.60$ was appropriate for $C_s = 0.18$ following their investigations of the link between C_s and C_w,

2.2 Reaction mechanisms for gas region

The pyrolysate PMMA is treated as methyl methacrylate (MMA) and its gaseous reaction is modelled as a one-step irreversible chemical reaction following Fernandez-Pello [2]:

$$C_5H_8O_2 + 6O_2 = 5CO_2 + 4H_2O. \tag{4}$$

The time averaged reaction rate for the mass fraction equation chemical species J $\bar{\omega}_J$ is expressed as

$$\bar{\omega}_J = (v_J'' - v_J')\frac{M_J}{M_{fu}}\bar{\omega}_{fu} \quad \text{kg/s/m}^3, \tag{5}$$

$$\bar{\omega}_{fu} = \bar{\rho}\min(\tilde{Y}_{fu}, \frac{\tilde{Y}_{O_2}}{s})/\tau_{reac} \quad \text{kg/s/m}^3, \text{ and} \tag{6}$$

$$\tau_{reac} = \min(\tau_{EDC}, \tau_{diff}) \quad \text{s}, \tag{7}$$

where v_J'' and v_J' are the molar stoichiometric coefficients of the right and left sides in reaction formula, M_J and M_{fu} are the molar weights of chemical species J and the fuel. $\bar{\omega}_{fu}$ is the time averaged reaction rate of fuel, $\bar{\rho}$ the time averaged density, $\tilde{Y}_{fu}$ and $\tilde{Y}_{O_2}$ are the density weighted mass fraction of fuel and O_2, s is the stoichiometric O_2-to-fuel mass ratio, τ_{reac} is the overall reaction time scale, τ_{EDC} is reaction time scale based on turbulent diffusion computed by the EDC model and τ_{diff} is the reaction time scale based on viscous diffusion. The combustion heat Δh_c of PMMA is set to 2.56×10^7 J/kg following Consalvi et al. [14]. In the flame spread scenario, both turbulent and laminar flame regimes exist. Near the pyrolysis wall and until 0.15–0.20 m from the leading edge [4,32], the flame is laminar. It goes through a transition process to be fully turbulent further away from the wall. In the laminar region, the EDC is not valid and the smaller one of the time scales in Eq. (7) is assumed to be dominant and chosen to calculate the reaction rate of the fuel.

2.3 The reaction time scale

τ_{EDC} is calculated as:

$$\tau_{EDC} = \frac{\overline{\rho}\min(\tilde{Y}_{fu}, \tilde{Y}_{O_2}/s)}{\overline{\omega}_{fu,EDC}} \qquad s, \tag{8}$$

where $\overline{\omega}_{fu,EDC}$ is the reaction rate computed by the extended EDC model for which more details can be found in Appendix B. The reaction time scale of laminar combustion is generally very small compared with the time step size Δt. This could cause numerical instability and often referred to as the stiffness problem [33]. For example, the Arrhenius expression for MMA is given as

$$\omega_{C_5H_8O_2} = A_{C_5H_8O_2}\rho^2 Y_{C_5H_8O_2} Y_{O_2} \exp(-T_{a,C_5H_8O_2}/T) \qquad kg/s/m^3, \tag{9}$$

where $A_{C_5H_8O_2} = 5.928\times10^9$ m^3/kg/s [14] and $T_{a,C_5H_8O_2} = 1.07\times10^4$ K [14], and T is the temperature. The kinetic reaction time scale near the stoichiometric condition is in the order of 10^{-5} s, and Δt is about 2×10^{-4} to 8×10^{-4} s in this study. Generally, the controlling time scale for laminar flame is the diffusion time scale the diffusion flux which enters each computational cell.

In the vicinity of the stoichiometric surface, the reaction rate for the mass fraction equation reactant specie J is obtained following Vervisch and Poinsot [34]:

$$\omega_J \approx -\overline{\rho}D(\nabla^2\tilde{Y}_J) = -\overline{\rho}D|\nabla Z|^2\left(\frac{d^2Y_J(Z)}{dZ^2}\right) \qquad kg/s/m^3, \tag{10}$$

where Z is the mixture fraction, $D|\nabla Z|^2$ is called the scalar dissipation rate [35], and $\overline{\rho}D(\nabla^2\tilde{Y}_J)$ is the same as the diffusion term of the mass fraction equation indicating the diffusion rate of $\tilde{Y}_J$ when flow is laminar. The reaction time scale τ_{diff} based on molecular diffusion in Eq. (7) was calculated based on $\overline{\rho}D(\nabla^2\tilde{Y}_J)$ in Eq. (10). In the oxygen rich side, the amount of fuel is less than that of

oxygen and fuel diffusion is hence the controlling time scale. Similarly, oxygen diffusion is the controlling time scale in the fuel rich side. These time scales τ_{diff} [s] are given as:

$$\tau_{diff} = \frac{\tilde{Y}_{fu}}{D(\nabla^2 \tilde{Y}_{fu})} \qquad Z_{st} > \tilde{Z}, \text{ and} \tag{11}$$

$$\tau_{diff} = \frac{\tilde{Y}_{O_2}/s}{D(\nabla^2 \tilde{Y}_{O_2})} \qquad Z_{st} \leq \tilde{Z}, \tag{12}$$

where $\tilde{Z}$ and Z_{st} are the density weighted mixture fraction and the stoichiometric mixture fraction.

2.4 Radiation model and estimation of mean beam length

FireFOAM solves the Radiative Transfer Equation (RTE) for non-scattering media with the Finite Volume Discrete Ordinates Method. For the gaseous radiation properties, the weighted sum of gray gas model (WSGGM) of Smith et al. [36] implemented into FireFOAM by Sikic et al. [27] is used. The total absorption coefficient including the soot contribution is calculated by

$$a_{tot} = a_g + a_S = -\frac{\ln(1-\varepsilon_{em})}{L_m} + C_{soot} f_v T \qquad \text{m}^{-1}, \text{ and} \tag{13}$$

$$f_v = \frac{\bar{\rho}\tilde{Y}_S}{\rho_S}, \tag{14}$$

where $C_{soot} = 1862$ m^{-1}K^{-1} following Consalvi et al. [14], a_{tot} is the total absorption coefficient, a_g the gas absorption coefficient, a_S the soot absorption coefficient, ε_{em} the emissivity obtained by WSGGM, f_v the volume fraction of soot, L_m the mean beam length and the density $\rho_S = 1800$ kg/m^3 [37]. Orloff et al. [38] assumed that the flame shape is a gas slab of width $2L_f$, height H_f, and thickness d_f, and the mean beam length L_m at the given height is estimated as

$$L_m = \frac{3.5 L_f d_f}{2L_f + d_f + 2L_f d_f / H_f} \qquad \text{m}, \tag{15}$$

where L_f is given as $W/2$. Following Orloff et al. [38], d_f is calculated from the PMMA height as:

$$d_f = \frac{x_{wall}}{16} \qquad \text{m}, \tag{16}$$

where x_{wall} is the height from the bottom of the PMMA wall. When the height of the assumed gas

slab is $x_{wall} = H_f$, the flame volume V_f can be approximated by $V_f \approx 2L_f \times H_f \times H_f / 16$ and $d_f = H_f / 16$.

V_f is computed following Yang et al. [39], who used the following criteria to determine the flame

border given as

$$R_o = \frac{1}{1 + s\tilde{Y}_{fu} / \tilde{Y}_{O_2}}, \tag{17}$$

where the C_3H_8 flame volume can be approximately defined when $0 \leq R_o \leq 0.99$. This criteria is

based on the flammability limit of C_3H_8. Since the theoretical amount of O_2 for $C_5H_8O_2$ is close to

that for C_3H_8, $0 \leq R_o \leq 0.99$ is used in this study.

Table 1 summarises the parameters/properties specified for the gas phase combustion.

Table 1 The gas phase model input parameters.

Gas phase model parameters	Values
Pr_t and Sc_t	0.85
C_w in the turbulence model	0.55 [30]
Combustion heat Δh_c	2.56×10^7 J/kg [14]
C_{soot} in the radiation model	1862 m^{-1}K^{-1} [14]
L_{sp} in the soot model	0.29 for CH_4 and 0.105 for $C_5H_8O_2$ [40].
Flame volume criteria	$0 \leq R_o \leq 0.99$ [39]

2.5 Pyrolysis model for the solid region and the interface boundary condition

The default pyrolysis model in FireFOAM, which is the 1-D diffusion equation for sensible

enthalpy with the Arrhenius type pyrolysis model developed by Chaos et al. [3] is adopted.

$$\frac{\partial \rho_{solid} h_{solid}}{\partial t} = \frac{\partial}{\partial y} \left(\lambda_{solid} \frac{\partial T_{solid}}{\partial y} - q_{dep} \right) - h_{solid}\omega_{solid} - \omega_{solid}(h_{mel} + h_{pyr} + h_{vap}), \tag{18}$$

where ρ_{solid} and h_{solid} are the solid density and sensible enthalpy, y is the coordinate, t the time, λ_{solid}

the solid heat conductivity, T_{solid} the solid temperature, q_{dep} the heat flux of in-depth radiation, ω_{solid}

the pyrolysis rate, h_{mel} the heat of melting, h_{pyr} the heat of pyrolysis and h_{vap} is the heat of

vaporization. For the transparent PMMA in the present study, ρ_{solid}, λ_{solid}, h_{pyr}, h_{mel}, and h_{vap} are 1150

kg/m^3 [41], 0.185 W/m/K [41], 8.4×10^5 J/kg [42], 1.8×10^5 J/kg [43] and 3.6×10^5 J/kg [43],

respectively. h_{solid} is defined by $h_{solid} = Cp_{solid}T_{solid}$, where Cp_{solid} is the mean specific heat at constant

pressure which is equal to 2270 J/kg/K. This value is the mean specific heat ranging from 293 to 750 K based on Kacem's [41] expression of the specific heat at constant pressure.

The definitions of h_{mel}, h_{pyr}, and h_{vap} are based on Wilde's study [43]. It assumes that once the material reaches the pyrolysis temperature, the PMMA starts melting and the pyrolysis reaction starts. Finally, the PMMA is vaporized to gas phase. The model does not separate the processes of melting, pyrolysis reaction and vaporization. The solid phase to gas phase shift is assumed as $PMMA \rightarrow C_5H_8O_2$. ω_{solid} is estimated by Arrhenius equation as

$$\omega_{solid} = \rho_{solid} A_{solid} \exp\left(-\frac{T_{as}}{T_{solid}}\right) \; \text{kg/m}^3\text{/s,} \tag{19}$$

where $A_{solid} = 3.92 \times 10^7$ 1/s [41] and $T_{as} = 1.3952 \times 10^4$ K [41].

For flame spread, the heat balance near the surface of the PMMA wall is an important factor. Some previous studies considered incident radiative heat flux only at the surface [14], and converted it to the heat fluxes into the solid phase. While some other studies suggested that in-depth radiation causes ignition delay [44,45]. The authors believe it should be taken into account. However, there still lacks information/data about the emissivity of PMMA and its effect on ignition. It would be outside the scope of the present study to resolve these issues, which can be revisited later when such information/data is available. In the present study, only absorption was accounted for by Beer's law [3,44,45] and radiative emissivity inside the PMMA was neglected. The heat flux of in-depth radiation q_{dep} due to absorption can be written as below using Beer's law :

$$q_{dep} = \eta_{solid} q_{rad} \exp(-a_{solid}\Delta_{dep}) \; \text{W/m}^2, \tag{20}$$

where η_{solid} is the transmissivity, q_{rad} the radiative heat flux, a_{solid} the solid absorption coefficient, and Δ_{dep} is the absolute value of the depth from the surface of the PMMA. In Eq. (20), q_{dep} decreases with an increase in Δ_{dep} because q_{rad} is absorbed in the PMMA. $a_{solid} = 1677$ m^{-1} [46] is used, and the PMMA transmits light up to approximately 91 to 93% [47]. η_{solid} is set to 0.91.

At the front interface between gas and solid, the boundary condition for h_{solid} is modelled as:

$$-\lambda_{solid} \frac{\partial T_{solid}}{\partial y} = \alpha_{solid} q_{rad} + \lambda_{Inter} \frac{(T_{First} - T_{solid,Inter})}{\Delta_{IF}} - \varepsilon_{solid} \sigma T_{solid,Inter}^4 \ , \tag{21}$$

where α_{solid} is the solid absorptivity, λ_{Inter} the thermal conductivity at the interface, T_{First} the gas temperature in the first cell along the front interface, $T_{solid,Inter}$ solid temperature at the interface, Δ_{IF} the distance from the centre of the first cell to the centre of the front interface cell, ε_{solid} the solid emissivity and σ is the Stefan Boltzmann constant. Generally, the transmissivity can be obtained as $\eta_{solid} = 1 - \alpha_{solid} - r_{solid}$. The reflectivity r_{solid} is approximately 0.035 to 0.08 [48]. r_{solid} is set to 0.04 and α_{solid} is hence 0.05. ε_{solid} is set to 0.95 following Consalvi et al. [14]. The second term of the right side in Eq. (21) is the convective heat flux q_c. Following Singh and Gollner [9], who suggested that using λ_{Inter} (=0.05 W/m K at 668 K) and temperature gradient at the wall as most appropriate to calculate the convective heat flux, $\lambda_{Inter} = 0.05$ W/m K at $T_{Inter} \approx 668$ K is used. The boundary condition of h at the front interface in the gas region is set as

$$T_{Inter} = T_{solid,Inter} \quad \text{K,} \tag{22}$$

where T_{Inter} the gas temperature at the interface.

At the rear surface of the PMMA, $\alpha_{solid} = \varepsilon_{solid}$ (=0.95) is assumed, and the boundary condition is given as

$$\lambda_{solid} \frac{\partial T_{solid}}{\partial y} = C |T_\infty - T_{solid}|^{1/3} (T_{solid} - T_\infty) + \varepsilon_{solid} (\sigma T_{solid}^4 - \sigma T_\infty^4) \ , \tag{23}$$

where $C = 0.152$ for a horizontal plane [49], $C = 0.131$ for a vertical plane [49].

At the front interface for the boundary condition of the momentum equation in the gas phase, the mass flow rate is estimated by the mass loss rate. The mass loss rate in each cell Ω_{solid} is given as:

$$\Omega_{solid} = \omega_{solid} V_{solid} \quad \text{kg/s,} \tag{24}$$

where V_{solid} is the cell volume in the solid region. The mass loss rate is calculated by adding all Ω_{solid} in the y direction. At each front interface cell in the gas region, the mass flow rate (= mass loss rate) m' is used as inlet for the momentum equation.

At the front interface, the boundary conditions for the mass fraction equations of gas species J and soot are evaluated from the fraction of the mass and diffusive fluxes at the first cells on the interface [18]. The boundary cells at the front interface are treated as a wall before pyrolysis occurs and changed to inlet following pyrolysis. The mass fraction at the front interface is given as:

$$Y_{Inter} = f_{conv} Y_{inlet} + (1 - f_{conv}) Y_{First} \,, \tag{25}$$

where Y_{Inter} and Y_{First} are the modified mass fraction at the interface and the mass fraction in the first cell from the interface, respectively; f_{conv} is the fraction of the effect of convection. Y_{inlet} is the inlet mass fraction at the front interface, where the value for $C_5H_8O_2$ is set to 1, and other species including the mass fraction of soot is set to 0. When $f_{conv} = 0$, $Y_{Inter} = Y_{First}$. The gradient of the mass fraction becomes 0, and the front interface is treated as the wall boundary condition. Similarly, when $f_{conv} = 1$, $Y_{Inter} = Y_{inlet}$; that is treated as the inlet condition. f_{conv} is evaluated by the ratio between the mass diffusive flux and mass flow rate. f_{conv} is given as

$$f_{conv} = \cfrac{1}{1 + \left| \cfrac{\bar{\rho}(D + v_{SGS} / Sc_t) / \Delta_{IF}}{m' / S_{Inter}} \right|} \,, \tag{26}$$

where D is the diffusion coefficient, and S_{Inter} is the surface area at the boundary cell. For the mass fraction of soot, f_{conv} is given as

$$f_{conv} = \cfrac{1}{1 + \left| \cfrac{\bar{\rho}(D_S + v_{SGS} / Sc_t) / \Delta_{IF}}{m' / S_{Inter}} \right|} \,, \tag{27}$$

where D_S is given as $D_S = 0.01D$ [25].

To take into account the influence of the surface regression length on the heat transfer, ρ_{solid} is set to constant but the grid size in the y direction changes by using the front interface as the reference coordinate. Thus, the rear surface moves when the grid size changes. The influence of the front interface decay on combustion in the gas region is not considered. However, since the distance from the front surface to the rear surface can be calculated, the time reaching the rear surface can be calculated and the change of the cell volume size ΔV_{solid} for each solid cell is computed following Pizzo et al. [8]:

13

$$\Delta V_{solid} = \frac{\omega_{solid} \Delta t}{\rho_{solid}} V_{solid} \quad \text{m}^3, \tag{28}$$

When all the mass in the cell is consumed, V_{solid} becomes close to 0. Therefore, the minimum V_{solid} is set to 5% of the initial V_{solid} for numerical stability and the pyrolysis rate in Eq. (19) is also set to 0. The surface regression length in each cell is computed as:

$$\delta_{solid,t+1} = \delta_{solid,t} + \frac{\Delta V_{solid}}{S_{solid}} \quad \text{m}, \tag{29}$$

where $\delta_{solid,t}$ is the surface regression length at t in each solid cell, S_{solid} is the normal face area to the y direction in each solid cell and the actual surface regression length δ_{solid} is estimated by adding all $\delta_{solid,t}$ in the y direction.

When the reaction rate is estimated by Eqs. (5)–(7) at the leading edge, the flame cannot be sustained. At the leading edge of the PMMA, the local pyrolysis rate and gaseous temperature are very high. Fuel and O_2 co-exist in the first cell due to strong air entrainment. The reduction in the temperature within the first cell is thought to be caused by insufficient grid resolutions here. To capture the reactive layer correctly by Eqs. (11) and (12), very fine grids are required between the wall and reactive layer, i.e. $\Delta y = 1.91$ mm is not sufficiently fine to capture the near wall reaction zone. The alternative way is using Eq. (9) but, as mentioned above, the stiffness problem would arise. To avoid the problem, the pyrolysis gas which comes from the leading edge is assumed to be consumed completely in the first cell. The amount of the pyrolysis gas in the first cell along the leading edge is expressed as $m' \Delta t / V_g \approx \bar{\rho} \tilde{Y}_{fu}$, where V_g is the cell volume in the gas region. This way, Δt (smallest available time scale) can be used as the reaction time scale because the pyrolysis gas vaporized from the wall with Δt.

The reaction rate at the leading edge is calculated from the oxygen consumption rate as

$$\bar{\omega}_{fu} = \bar{\rho} \frac{1}{\Delta t} \min(\tilde{Y}_{fu}, \frac{\tilde{Y}_{O_2}}{s}). \tag{30}$$

τ_{reac} at the leading edge is given as

$$\tau_{reac} = \frac{\overline{\rho}\tilde{Y}_{fu}}{\overline{\omega}_{fu}} = \frac{\tilde{Y}_{fu}}{\min(\tilde{Y}_{fu}, \tilde{Y}_{O_2}/s)}\Delta t ,\qquad(31)$$

where the time scale is applied to only the first bottom cells along the PMMA wall to avoid the influence of Δt. The maximum Δt was set to 0.0008 s in this study to sustain the flame at the leading edge. The influence of Eq. (31) will be discussed in section 3.3. The overview of the flame spread model and parameters are shown in Fig. 1 and Table 2, respectively.

Table. 2 The pyrolysis model parameters

Parameters	Values
Density ρ_{solid}	1150 kg/m^3 [41]
Solid heat conductivity λ_{solid}	0.185 W/m/K [41]
Mean specific heat at constant pressure Cp_{solid}	2270 J/kg/K [41]
Heat of vaporization h_{vap}	3.6×10^5 J/kg [43]
Heat of melting h_{mel}	1.8×10^5 J/kg [43]
Heat of pyrolysis h_{pyr}	8.4×10^5 J/kg [42]
Pre-exponential factor A_{solid}	3.92 × 10^7 1/s [41]
Activation temperature T_{as}	1.3952 × 10^4 K [41]
Absorption coefficient a_{solid}	1677 m^{-1} [46]
Transmissivity η_{solid}	0.91 [47]
Reflectivity r_{solid}	0.04 [47,48]
Absorptivity α_{solid}	0.05 ($\eta_{solid} = 1 - \alpha_{solid} - r_{solid}$)
Emissivity ε_{solid}	0.95 [14]
Interface heat conductivity λ_{Inter}	0.05 W/m K at $T_{Inter} \approx 668$ K [9]
C (for the rear surface condition)	0.152 for a horizontal plane 0.131 for a vertical plane [49]

3 Results

For model validation, the experiments of Pizzo et al. [8], Singh and Gollner [8] and Liang et al. [10] have been simulated. Figure 2 shows a sketch of the computational domain for all the cases while the actual dimensions for each case are different. In the coordinate, $x = 0$ is set to the bottom of the gas region, $y = 0$ is the interface between the gas and solid regions, and $z = 0$ is the centre of the PMMA wall. It should be noted that $x_{wall} = x - x_a$ as shown in Fig. 2.
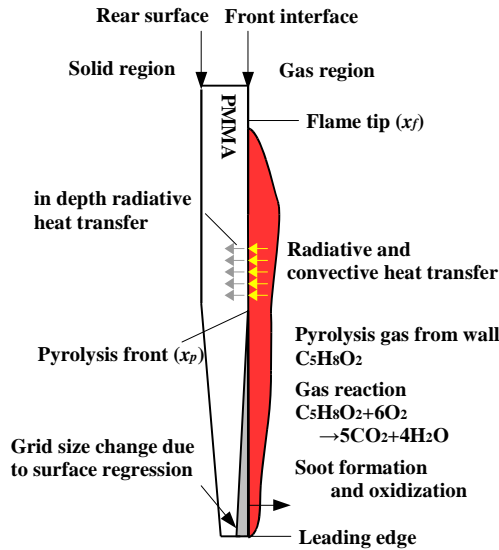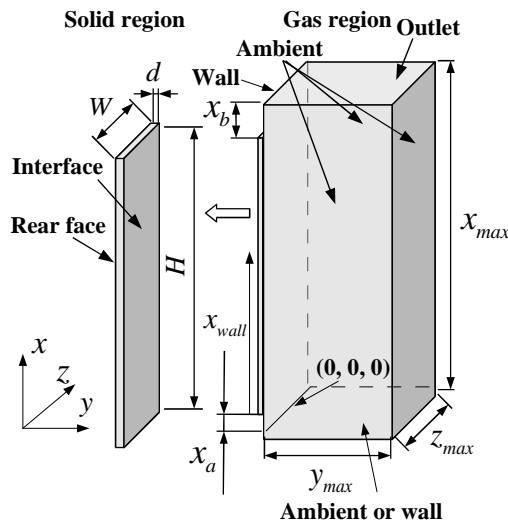
15

Fig. 1 Overview of the flame spread model

Fig. 2 The computational domain.

3.1 Validation of the pyrolysis model

A decoupled simulation was conducted without the gaseous region to validate the pyrolysis model

and its parameters with the three experiments of Pizzo et al. [8] which consisted three case. For the

first cases, radiative heat fluxes of 14 (Case A) and 18 kW/m^2 (Case B) were imposed on the PMMA

surface. For the third Case C, the sample was subjected to a mean heat flux of 24.5 kW/m^2 imposed

by the flame to give the flaming condition [8]. The PMMA sample was 0.1 (W) × 0.1 (H) and 0.03

(d) m and set horizontally. For Cases A and B, the radiative flux was imposed on the front interface

16

as shown in Fig. 1. For Case C, 24% of the radiative flux and 76% of the convective heat flux were given as the boundary condition to mimic the flaming condition following Singh and Gollner [9].
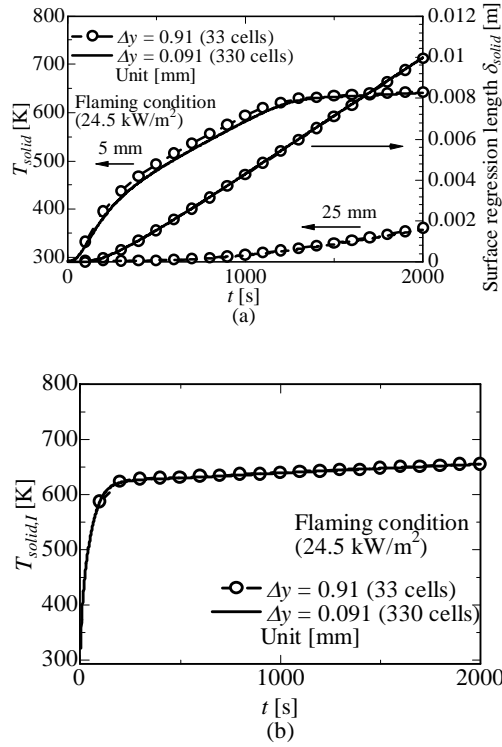
Fig. 3 Comparison of the predicted (a) T_{solid} and surface regression δ_{solid}
and (b) $T_{solid,Inter}$ by different grid resolutions in the solid region.

Figure 3 (a) shows the comparison of the surface regression length δ_{solid} and temperature T_{solid} *vs* time at depths of 5 and 25 mm from the surface with different grid resolutions. At 5 mm, the predicted T_{solid} was slightly different between $\Delta y \approx 0.91$ and $\Delta y \approx 0.091$ mm, and the error is about 1.5 %. The error "*Err*" is evaluated based on the standard deviation [50] between 0 s to 2000 s as

$$
Err = \frac{\left[\sum_{N=1}^{N_{max}} (\phi_{ref,N} - \phi_N)^2 \right]^{1/2}}{\phi_{ref,max} N_{max}} \times 100 \quad \% ,
\tag{32}
$$

where N is the number of the data, N_{max} is the maximum number of the data, $\phi_{ref,N}$ is the N_{th} reference data, ϕ_N is the N_{th} compared data, and $\phi_{ref,max}$ is the maximum reference data to scale

the value. Also, δ_{solid} predicted by $\Delta y \approx 0.91$ and $\Delta y \approx 0.091$ mm is very close, and *Err* is about 0.37 %. Hence, $\Delta y \approx 1$ mm has been used is used in the subsequent simulations. δ_{solid} is related to the mass flow rate m'. Figure 3 (b) shows the solid temperature at the interface $T_{solid,Inter}$ *vs* time with the different grid resolutions. $T_{solid,Inter}$ affects the interface between the fluid and solid region in Eq. (21). $T_{solid,Inter}$ predicted by the two different resolutions are in good agreement, and the *Err* is about 0.23 %. Based on these comparisons, $\Delta y \approx 0.91$ is hence chosen for the subsequent simulations.

Figure 4 shows comparison of the surface regression length δ_{solid} and temperature T_{solid} *vs* time at depths of 5 and 25 mm from the surface. A uniform mesh with $\Delta y \approx 0.91$ mm was used in the *y* direction. For Case A, the predicted δ_{solid} is in very good agreement with the experimental data and earlier predictions of Pizzo et al. [8] and Kacem et al. [12]. For Case B, the predicted δ_{solid} is slightly lower than the measurements and the predictions of Pizzo et al. [8]. As commented by Pizzo et al. [8], considering that the bubble size appeared in the surface was about 1 mm, a discrepancy within 1 mm should be considered as satisfactory. When $t > 2000$ s, the discrepancy is within 1 mm while it is bigger than 1 mm at $t = 2500$ s. Assuming 1 mm discrepancy, the error of δ_{solid} is 10.8%, while that is 10.9% in this simulation.

For Case C, the prediction is close to that of Kacem et al. and within 1 mm of the measurements until 1700 s simulation. Assuming 1 mm discrepancy, the error of δ_{solid} is 12.5% between $t \approx 250$ to 2000 s. The error is about 11.5% between $t \approx 250$ to 2000 s but the discrepancies between the predictions and measurement are slightly large after 1700 s. The result implies that the discrepancy of δ_{solid} is slightly large under the flaming condition after 1700 s. As the time scale of the flame spread stage is about $t \approx 505$ s for 1 m height of the PMMA [10], the error would only have minimum influence on the flame spread simulation.

The predictions of Pizzo et al. [8] were in closer agreement with the measurements but they used different pre-exponential factor for Case C from that for Cases A and B while both Kacem et al. [12]

and the present study used the same parameters in all the cases. These comparisons demonstrate that the current model captured the trend of δ_{solid} reasonably well.
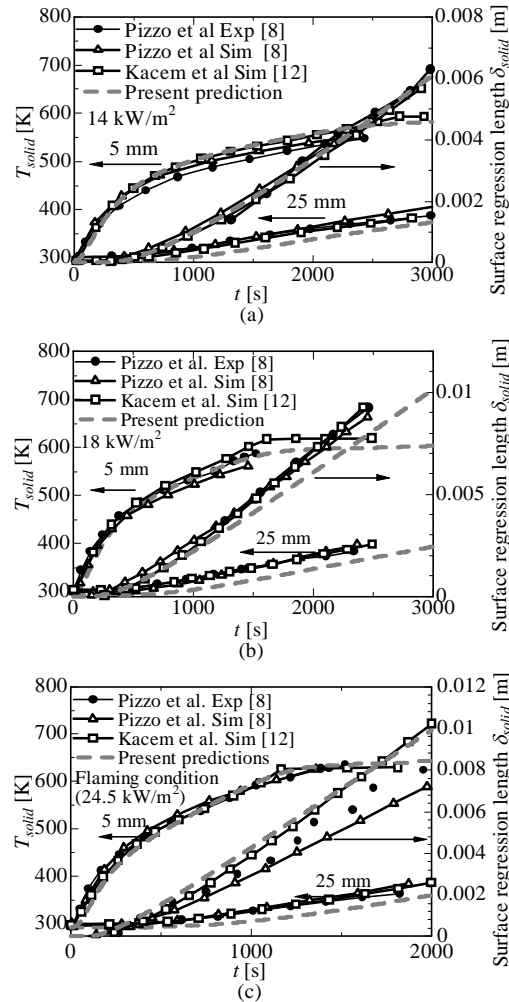

Fig. 4 The predicted and measured T_{solid} and surface regression length δ_{solid} vs time.

As also shown in Figs. 4 (a)–(c), at 5 mm depth, the predicted temperature profiles are in excellent agreement with the measurements for Cases B and C while the model slightly over-predicted the temperatures for Case A. Overall the maximum discrepancies are about 4% for Case A. At 25 mm depth, the proposed model under-predicted the measurements while the predictions of Pizzo et al. [8] and Kacem et al. [12] were in good agreement with the experimental data. This is thought to be due to the fact that the present study used the constant specific heat while Kacem et al. [12] and Pizzo et al. [8] used the specific heat calculated by the polynomial coefficient depending on T_{solid}.

19

Nevertheless, the discrepancy incurred by this simplification should not affect the predictions of the flame spread rate which is determined by the time reaching the pyrolysis temperature (about 580 K at 0.5 mm depth in this study) as T_{solid} at 5 mm was close to the experimental data.

3.2 Determination of the cell size

In order to establish the desired grid resolutions, numerical test were conducted using the experimental set up of Saito et al. [6] as reference but shorter PMMA was used to reduce the computational time. The entire process of this case from pilot burner combustion to flame spread was previously simulated by the authors [28]. Here only the ignition procedure was computed to help identifying the desired grid resolution for the subsequent test cases.

The geometry is the same as that shown in Fig. 2 while the specific dimensions are: $H = 0.5$ m, $W = 0.3$ m, $d = 0.013$ m, $y_{max} = 0.2$ m, $x_{max} = 0.5$ m, $z_{max} = 0.36$ m, $x_a = 0$ m and $x_b = 0$. m. The solid region has 13 uniform cells in the y direction.

The pilot methane burner was set at the bottom of the geometry along the PMMA wall. It was 0.04 m in the y direction and 0.3 m in the z direction. As a CH_4 burner was used to ignite the PMMA wall in some of the experiments, a one-step irreversible chemical reaction is expressed as

$$CH_4 + 2O_2 = CO_2 + 2H_2O, \tag{33}$$

The heat release rate was taken from the experimental measurements as 22.7 kW/m and converted to the mass flow rate of the methane gas. The data are averaged between $t = 10$ to 30 s. Its heat release rate of 22.7 kW/m is approximately the same as q' at $x_p = 0.2$ m. The burner fires on the wall were sometime used to discuss the total heat flux with that of the flame spread or wall fire cases [14,51].

Figures 5 (a), (b) and (c) show q_c q_{rad}, and q_{tot} vs height at the centre of the PMMA. The grid size in the y direction is not uniform. Δy is the first cell size from the wall surface, and the expansion ratio is set to 3.6% . q_{tot} is given as $q_{tot} = q_c + q_{rad}$, where $q_c = \lambda(T_F - T_{solid})/\Delta_{IF}$, and q_{rad} is obtained by the solution of RTE in FireFOAM. Ren et al. [19] found in their study that a resolution of 3 mm was

needed for the first cell from the wall to obtain the approximately grid independent predictions. Δy = 1.91 mm was set to in the present study.
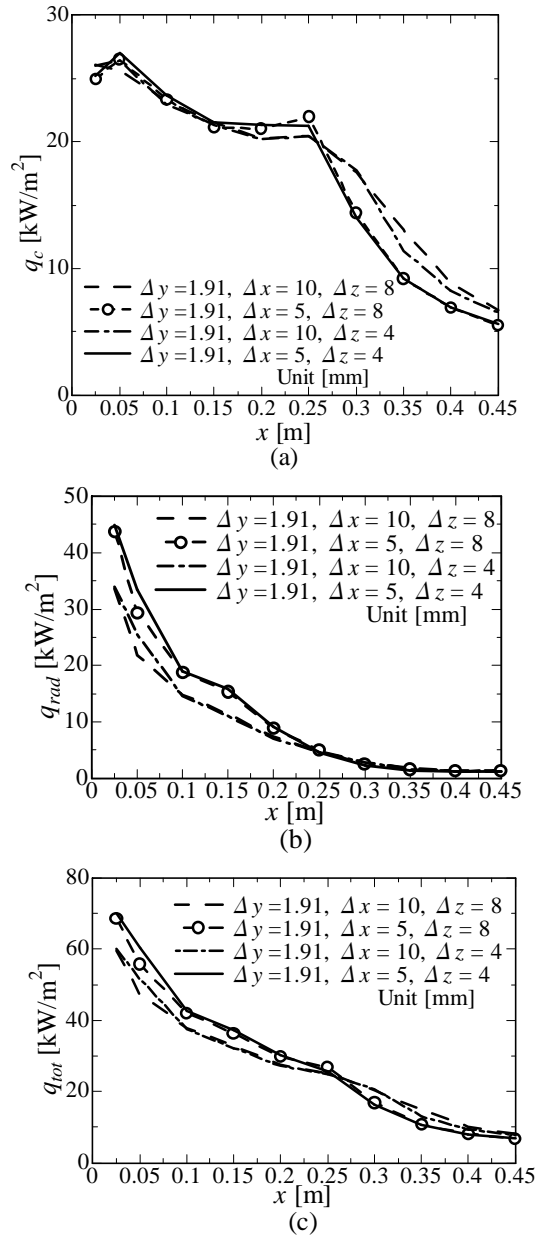

Fig. 5 Comparison of the predictions with different grid resolutions.
(a) convective, (b) radiative and (c) total heat fluxes (q_c, q_{rad}, and q_{tot}) *vs* height.

It can be seen from Figs. 4 (a) and (b) that the effect of Δz is smaller than that of Δx which is parallel to the direction of gravity. The predicted q_c, q_{rad}, and q_{tot} with Δy = 1.91 mm, Δx = 5 mm, and Δz = 4 mm are very similar to those with Δy = 1.91 mm, Δx = 5 mm and Δz = 8 mm. Therefore,

in the subsequent test cases, $\Delta y \approx 1.91$ mm, $\Delta x = 5$ mm, and $\Delta z = 8$ mm are used, and the expansion ratio is set up to 4% in the y direction to maintain the same grid resolution.
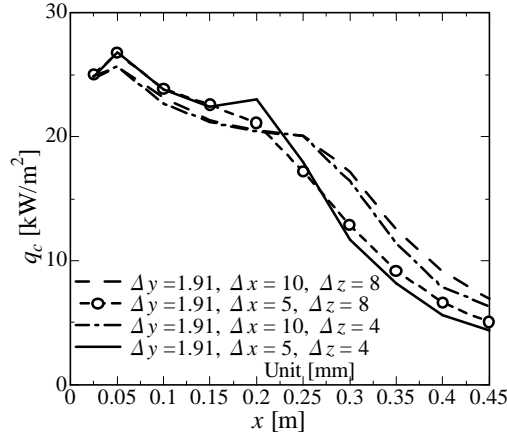
Fig. 6 The convective heat flux q_c when τ_{diff} is given as $\tau_{diff} = 0.1\Delta_{filter}^2 / D$ [19].

Figure 6 shows the predicted q_c when τ_{diff} is given as $\tau_{diff} = 0.1\Delta_{filter}^2 / D$ [19]. The predicted q_c with $\Delta y = 1.91$ mm, $\Delta x = 5$ mm, and $\Delta z = 4$ mm is slightly different from those with $\Delta y = 1.91$ mm, $\Delta x = 5$ mm and $\Delta z = 8$ mm but those were close in the present prediction as mentioned above. This indicates that the use of Eqs. (11) and (12) improved the grid independency.

3.3 Validation of small scale flame spread and wall fire tests and model sensitivity tests

This section describes validation with the small scale flame spread of Huang and Gollner [52] as well as the wall fire tests of Singh and Gollner [9]. Some sensitivity studies have also been conducted with the former case about the ignition conditions and with the second case about radiation treatment, reaction time scale expression and Courant number.

For the case of Huang and Gollner [52], the respective dimensions in relation to Fig. 2 are: $H = 0.2$ m, $W = 0.104$ m, $d = 0.013$ m, $y_{max} = 0.2$ m, $x_{max} = 0.45$ m, $z_{max} = 0.152$ m, $x_a = 0.05$ m, and $x_b = 0.2$ m. In the solid region, the number of cells was set to 13 cells uniformly in the y direction. The ambient condition was set on the floor in Fig. 2. Following Ren et al. [19], the first grid size from the wall was set to $\Delta y = 1.98$ mm, and also, $\Delta x = 5$ mm and $\Delta z = 8$ mm were used. In the solid region,

22

the number of cells was set to 13 cells uniformly in the y direction (initial $\Delta y = 1$ mm). In the experiment, the ignition was started at the bottom by a small ceramic wick soaked with 3 mL of methyldecanoate. During the ignition, the whole PMMA surface except for the bottom 2 cm was covered by a 6 mm thick sheet of ceramic insulation [52]. In this simulation, the Ignition was achieved by imposing 45 kW/m^2 radiative heat flux at $0 \leq x_{wall} \leq 0.02$ m until $t = 65$ s. After the ignition was established, the time was reset to $t = 0$ s.

The flame height x_f is related to the heat release rate and geometric configuration [53]. In this study, it is computed by the highest location where stoichiometric mixture exists following [25,26], i.e. $x_f = \max(x - x_a)$ when $\tilde{Y}_{fu} - \tilde{Y}_{O_2}/s \geq 0$, where $\max(x - x_a)$ represents the maximum coordinate from the bottom of the PMMA in the x direction. The definition of the pyrolysis front is dependent on the investigators. Saito et al. [6] defined the pyrolysis temperature as 593 ± 25 K within $y = -1$ mm from the PMMA wall, Huang and Gollner [52] defined the pyrolysis front as $T_{solid} = 573$ K at the PMMA wall surface, Tsai [54] determined it as $T_{solid} = 623$ K and Consalvi et al. [55] used the $T_{solid} = 630$ K in their model. The consensus of these previous studies is that the pyrolysis front should be determined by the PMMA temperature. However, because of the different temperature values used by the aforementioned experimentalists in the definition of the pyrolysis front, the pyrolysis temperature should be determined for comparison with each test set. Thus, the pyrolysis height is defined as the centre of the PMMA reaching $T_{solid} = 580$ K at -0.5 mm depth from the surface in order to match the measured x_p in this simulation.

Figure 7 shows the predicted and measured pyrolysis x_p and flame heights x_f *vs* time. The predicted x_p is slightly underestimated at $t < 230$ s, and overestimated at $t \geq 230$ s. Also, the predicted x_f is in reasonably good agreement with the experimental data at $t < 230$ s, but overestimated at $t \geq 230$ s. The flame spread rate in the experiment was 6.7×10^{-5} m/s [52], and the computational result is 6.87×10^{-5} m/s with the different being about $Err = 2.5\%$.
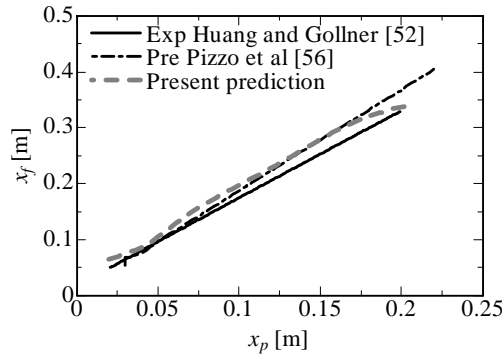
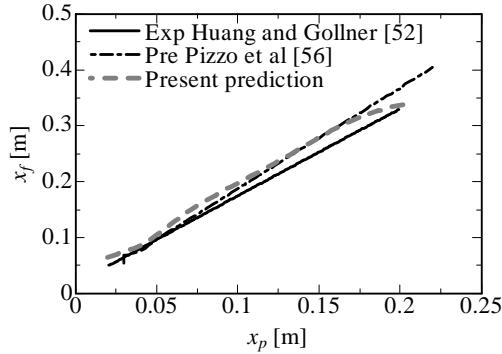Fig. 7 The predicted and measured pyrolysis x_p and flame heights x_f vs time.

Fig. 8 The predicted and measured flame height x_f vs pyrolysis height x_p.

Figure 8 shows the predicted and measured flame height x_f vs pyrolysis height x_p. Pizzo et al.'s [56] predictions based on the modified mass transfer number is also plotted for comparison. The predicted data is slightly higher than the experimental data but very close to the predictions of Pizzo et al.

Figure 9 shows the iso-surfaces of the flame volume defined using the criteria $R_o = 0.99$ in Eq. (17). It can be seen that the flame volume gradually expands as time passes. When $x_p \approx 0.05$ m, the flame is laminar. After $x_p \approx 0.15$ m, the flame volume shape changes at $0.15 \leq x_{wall} \leq 0.2$ m.

Using the dimensionless parameter $\xi = (x_{wall} - x_p) / (x_f - x_p)$, Consalvi et al. [14] divided the turbulent diffusion flame on the PMMA surface into three regions, i.e. the continuous flame (CF) $\xi < 0.4$, intermittent flame (IF) $0.4 \leq \xi \leq 1.6$, and plume (PL) region $\xi > 1.6$. The three regions are depicted for the iso-surface plot at $t = 165$ s in Fig. 9. The continuous flame region is located between the leading edge and slightly upward position of x_p, and the end of the intermittent flame

24

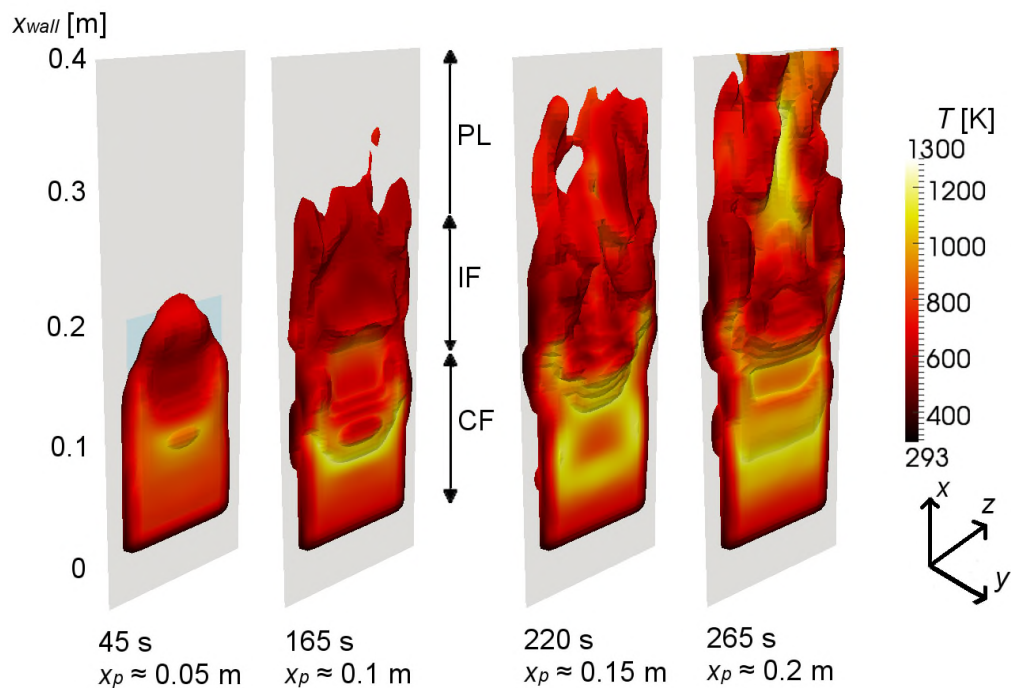region is positioned almost equal to the top of the flame volume. There is no visible flame in the plume region.

Fig. 9 The predicted iso-surfaces of the flame volume defined as the criteria $R_o = 0.99$. The continuous flame (CF), intermittent flame (IF), and plume (PL) regions are marked out at 165 s.
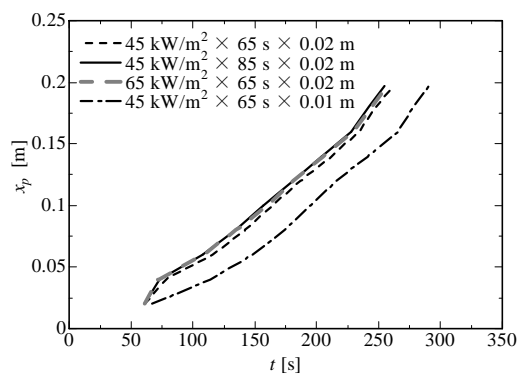

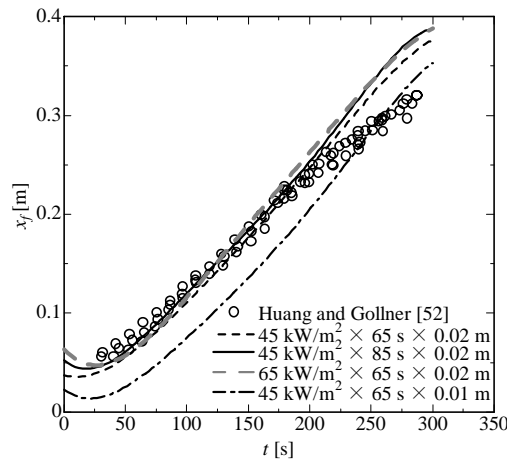Fig. 10 The predicted pyrolysis height x_p vs time with different ignition conditions.

Fig. 11 The predicted flame height x_f *vs* time with different ignition conditions.

Sensitivity studies have been conducted on different ignition conditions, which involve the imposing radiative heat flux, heating time, and heating height. As can be seen from Fig. 10, significant difference happens when the different heating height (0.01 m) is used. In the case of (45 kW/m^2, 65 s, 0.01 m), the initial heat release rate from the PMMA wall is 50% compared with that of (45 kW/m^2, 65 s, 0.02 m). This is thought to be the reason why the flame spread is very slow in the former case. Similarly, the predicted x_f is also significantly different as shown in Fig. 11. However, this also means that the heating height can be determined from x_f at the early stage if it is not given so that the initial conditions can be better set to mimic the actual experimental scenario.
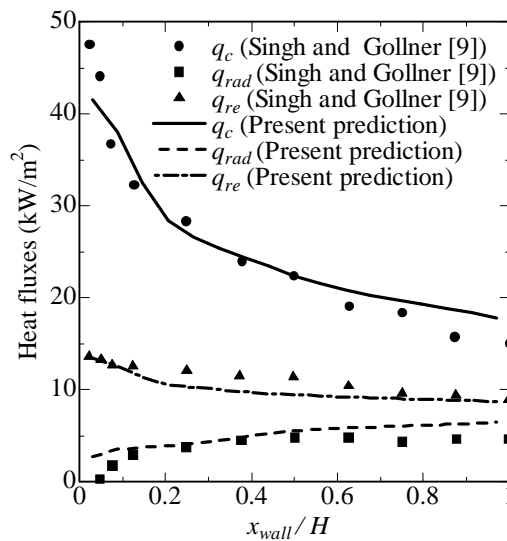

Fig. 12 The predicted and measured heat fluxes *vs* dimensionless height x_{wall}/H.

26

To validate the model for q_c, q_{rad}, and q_{re}, the small scale wall fire of Singh and Gollner [9] was computed. The respective dimensions in relation to Fig. 2 are: $H = 0.085$ m, $W = 0.084$ m, $d = 0.0127$ m, $y_{max} = 0.1$ m, $x_{max} = 0.335$ m, $z_{max} = 0.132$ m, $x_a = 0.05$ m, and $x_b = 0.2$ m. In the solid region, the number of cells was set to 13 cells uniformly in the y direction. The ambient condition was set on the floor in Fig. 2. Following Ren et al. [19], the first grid size from the wall was set to $\Delta y = 1.94$ mm, and also, $\Delta x = 5$ mm and $\Delta z = 6$ mm were used. In the experiment, the ignition was made by a blowtorch passed over the surface. For simplicity, the Ignition was achieved by imposing 45 kW/m^2 radiative heat flux until $t = 65$ s. After ignition was established, the time was reset to $t = 0$ s. The results were taken from $t = 260$ s to 310 s. This time was chosen in order to match the local pyrolysis rate in the downstream region.

Figure 12 shows the heat fluxes vs the dimensionless height calculated as x_{wall} / H. The predicted convective, radiative, and re-radiative heat fluxes (q_c, q_{rad}, and q_{re}) are close to the measurements. Generally, q_c is higher than q_{rad}, and also very high q_c is observed at the leading edge of the PMMA wall.

Sensitivity tests have also been conducted for different radiation sub models including that of Consalvi et al. [14] who estimated the gas absorption coefficient a_g as $a_g = 0.1X_{pr}$, where X_{pr} is the mole fraction of products; the RADICAL program [57] which expressed as the poly-nominal expression and the grey formulation of the Smith et al.'s WSGGM [36] used in the present prediction. In this comparison, apart from changing the radiation treatment, all other models components and parameters were kept the same. As shown in Fig. 13, the present prediction using WSGGM is in better agreement with the experimental data than q_{rad} obtained by the other radiation sub models.
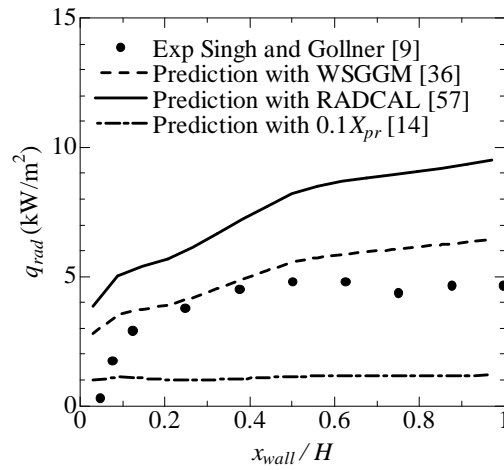
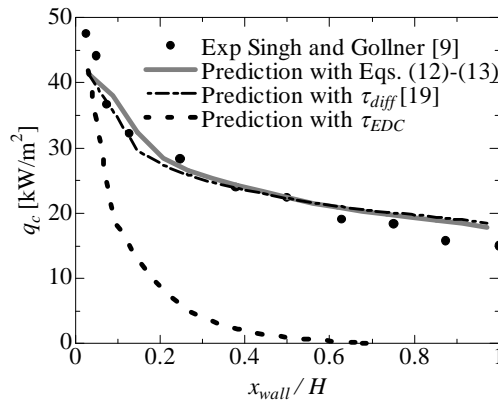Fig. 13 Sensitivity tests for radiation sub-models.

Fig. 14 Sensitivity tests for the reaction time scale expressions.

Figure 14 shows the sensitivity tests for the reaction time scale expressions. Using different τ_{diff} gives almost the same q_c, which are very different from the result if τ_{EDC} is used. This is because the EDC model is not applicable for the laminar region. It is important in flame spread simulations to use the reaction time scale modified by Eq. (7).
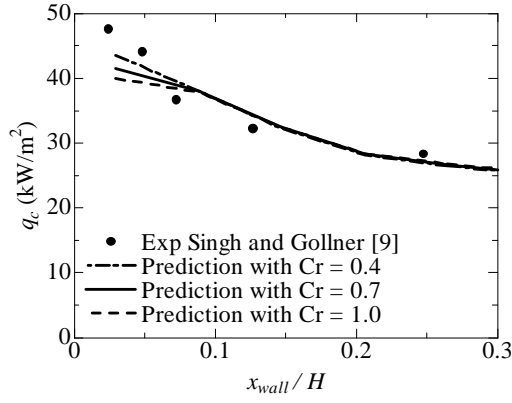
Fig. 15 The measured (Exp) and predicted convective heat fluxes q_c vs dimensionless height x_{wall}/H depending on using Eq. (31) and Courant number (C_r).

Figure 15 shows the measured and predicted q_c when different Courant number C_r was used. When the leading edge modification in Eq. (31) is not used, extinction occurred because of lack of q_c at the leading edge. Figure 17 also shows the obvious influence of Δt on q_c at the leading edge. Δt is about 0.001, 0.0007 and 0.0004 s when Cr = 1.0, 0.7 and 0.4, respectively. It is clear that without Eq. (31), the Courant number and time step would have noticeable influence on the predictions at the leading edge while the downstream region is unaffected.

3.4 The analysis of the soot distribution

To validate the model for the soot volume fraction f_v, the wall fire of Hebert et al. [58] was computed. In the experiments, the PMMA size was originally 0.45 (H) × 0.25 (W) × 0.03 (d) m but the front side of the PMMA wall was covered with a thick steel frame to avoid unnecessary flame spread. Hence, the actual size became 0.4 (H) × 0.2 (W) × 0.03 (d) m. The total duration of the experiment was 3000 s. The f_v profiles were measured at 0.28 and 0.36 m from the bottom of the thick steel frame at 1810 and 2070 s. The laser sheet was set at 0.05 m from the left edge. The five measurements quoted were performed with different laser fluencies.

In the simulation, the respective dimensions in relation to Fig. 2 are 0.4 (H) × 0.2 (W) × 0.03 (d) m, y_{max} = 0.25 m, x_{max} = 0.96 m, z_{max} = 0.248 m, x_a = 0.05 m and x_b = 0.505 m. The predicted values are obtained at x_{wall} = 0.255 m and 0.335 m because the steel frame height set at the bottom of the

29

PMMA wall was 0.025 m. In the solid region, the number of cells was set to 30 cells uniformly in the *y* direction (initial $\Delta y = 1$ mm). The ambient condition was set on the floor as shown in Fig. 2. The first grid size from the wall was set to $\Delta y \approx 2$ mm, $\Delta x = 5$ mm and $\Delta z = 8$ mm were used.
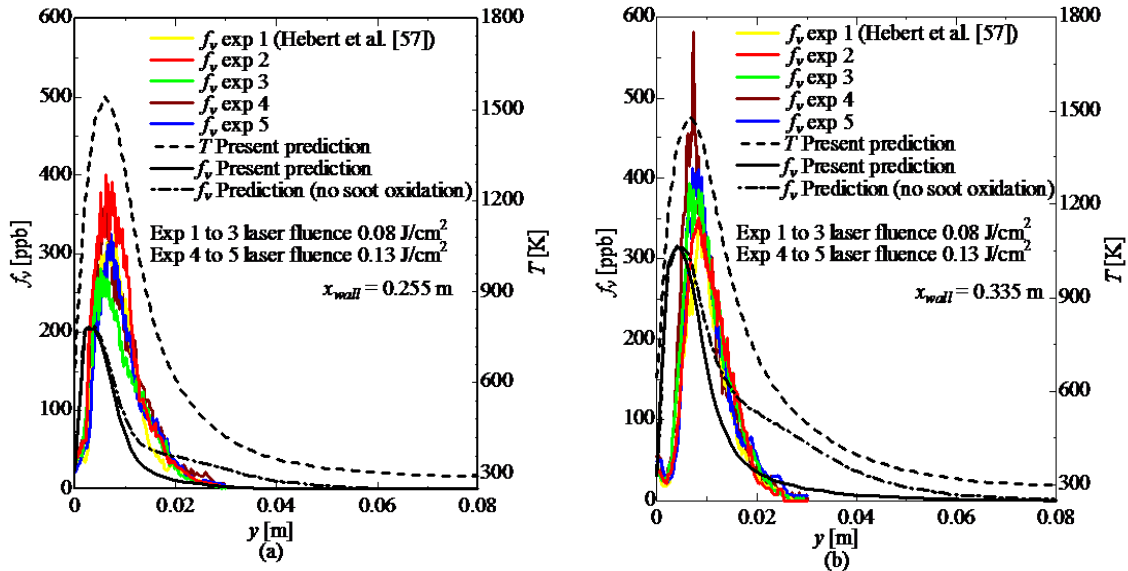

Fig. 16 The predicted mean soot volume fraction (f_v) and temperature profiles *vs* distance from the PMMA wall *y* at (a) $x_{wall} = 0.255$ and (b) $x_{wall} = 0.335$ m.

Although the initial period of these tests involved flame spread, later on from 1800 s, it was essentially a PMMA wall fire. Figure 16 shows the predicted mean f_v and temperature profiles *vs* the distance from the PMMA wall *y* averaged from 1800 to 1840 s. The predicted peak soot volume fraction f_v is in reasonably good agreement with the experimental data, while the peak position of f_v is slightly different from the experimental data. The predicted peak f_v is located closer to PMMA wall in comparison with the location for the peak temperature. For $x_{wall} = 0.255$, the maximum f_v was between 250 to 450 ppb in the five measurements of Hebert et al. [58] and 207 ppb in the present prediction; for $x_{wall} = 0.355$, the measured peak were between 250 and 450 ppb [58] while the predicted peak is 317 ppb.

As may be seen from the updated Fig. 16, without the soot oxidation model, the soot volume fraction f_v is slightly over-predicted at $y > 0.02$ m. The predicted peak value is however closer to that

predicted with the soot oxidation model. According to Chen et al. [25], the influence of the soot

oxidation model is negligible when turbulence is low. For the cases studied here, turbulence is weak

and the effect of soot oxidation model is minor.

3.5 Large scale flame spread scenarios

This section starts with validation of the large scale flame spread scenario tested by Liang et al.

[10] followed by analysis of the detailed field predictions of the unsteady phenomena as well as

comparison with some published correlations.

Liang et al. [10] investigated the influence of the altitude on flame spread, and the experimental

data were measured in Hefei and Lhaca. In this study, the experimental data measured in Hefei

where the altitude is 29.8 m was used. The specific dimensions with reference to Fig. 2 are: $H =$

1.005 m, $W = 0.296$ m, $d = 0.01$ m, $y_{max} = 0.6$ m, $x_{max} = 1.6$ m, $z_{max} = 0.36$ m, $x_a = 0.01$ m and $x_b =$

0.585 m. In the experiment, the bottom of the PMMA was ignited using a twisted cotton rope soaked

in ethanol. For simplicity, the ignition was achieved by imposing 45 kW/m^2 radiative heat flux until

65 s at $0.01 \leq x \leq 0.06$ m in the current simulation. The length of the ignition region was chosen in

order to fit the measured x_f. In the solid region, the number of cells was set to 10 cells uniformly in

the y direction (initial $\Delta y = 1$ mm). Following Ren et al. [19], the first grid size from the wall was

set to $\Delta y = 1.99$ mm, and $\Delta x = 5$ mm and $\Delta z = 8$ mm were used. The wall condition was set on the

floor in Fig. 2. A total of 1,555,200 cells for the gas region and 74,370 cells for the solid region were

used, respectively. The same grid resolutions are maintained in the simulations of the Liang et al.

experiments as in the smaller configuration of Saito et al., i.e. overall a much larger number of

computational grids are used for the bigger case.

Figure 17 shows the pyrolysis height (x_p) and flame height (x_f) vs time. The pyrolysis height is

defined as the centre of the PMMA reaching $T_{solid} = 580$ K at 0.5 mm depth from the surface in order

to fit the measured x_p as shown in Fig. 17. Consalvi et al. [14] pointed out that the definition of the

pyrolysis temperature gave different x_p *vs* time, and also the definition of the value of the pyrolysis temperature varied from one experiment to another. The reference data was obtained from Liang et al. [10]. In comparison with the measurements, the predicted x_p and x_f are in reasonably good agreement with the measurements. The flame spread reached the top of the PMMA when $t \approx 515$ s in this simulation while that was about 505 s in the experiment. Preliminary predictions with a shorter ignited region resulted in slower increase of x_p. However, the increase patterns of x_p and x_f followed the same trend.
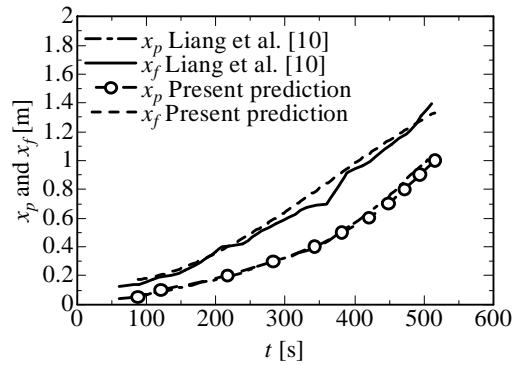

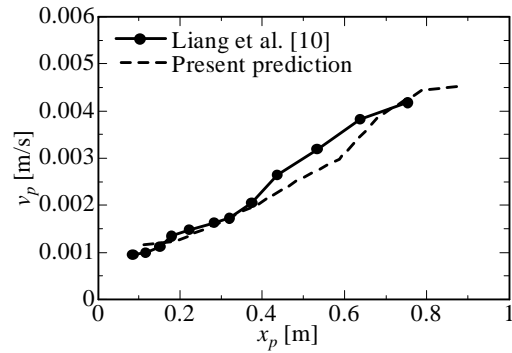Fig. 17 The predicted and measured pyrolysis (x_p) and flame (x_f) heights *vs* time

Fig. 18 The flame spread rate v_p *vs* pyrolysis height x_p.

As can be seen in Fig. 18, the predicted v_p is almost constant when $x_p < 0.2$ m, and increases almost linearly at $0.2 < x_p < 0.6$ m. At $0.6 < x_p < 0.7$ m, the predicted v_p rapidly increases, and comes close to the experimental data at $x_p > 0.7$ m. This tendency was observed at $0.4 < x_p < 0.5$ m in the experiment. The predicted time for the pyrolysis front to reach the top of the PMMA wall differs by about 10 s. The maximum *Err* here is about 7.9% based on Eq. 32.
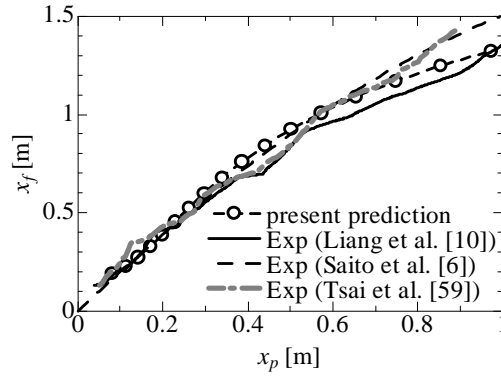
32

Fig. 19 The predicted and measured flame height x_f vs pyrolysis height x_p.

The predicted and measured x_f vs x_p is shown in Fig. 19. The predicted data is reasonably close to Liang et al.'s experimental data. x_f is correlated with x_p, and that was given as $x_f = K_p x_p^m$ [4], where K_p and m is the fitted coefficient. The measurements of Saito et al. [6] and Tsai et al. [59] are also plotted here for reference, but it should be noted there were no side walls in these tests and the PMMA width was 0.3 m. Tsai et al.'s expression of x_f takes into account the effect of the PMMA width as $x_f = K_p x_p^m W^{0.2}$, where $K_p = 1.65$ and $m = 0.67$. Besides, Delichatsios [51] predicted $K_p = 1.78$ and $m = 0.802$, and Orloff et al. [4] reported $m = 0.781$. In this study, $K_p = 1.45$ and $m = 0.752$ can be obtained from in Fig. 19. These comparisons support the wide applicability of $x_f = K_p x_p^m$ for situations with or without side walls while m falls into almost between 2/3 to 0.8.

Figure 20 shows the $(x_f - x_p)$ vs time. This represents the pre-heating length between x_p to x_f. The pyrolysis height x_p is 0.005 m when $t < 85$ s because the flame spread did not occur until this time. Further, since the maximum height of the PMMA sample was 1 m, x_p is 1 m when $t > 515$ s. As can be seen in Fig. 20, the prediction follows well the trend of the measurements. As expected, $(x_f - x_p)$ increases with time. Hence, v_p gradually increases as discussed in Fig. 18. The preheating length $(x_f - x_p)$ starts to decrease after the peak because the pyrolysis front becomes a convex shape as reflected in the temperature contours on the surface of the PMMA in Fig. 21. In such circumstances, x_f decreases with the decreases in the heat release rate per sample width q'. The correlation between x_f and q' is discussed in Fig. 23.
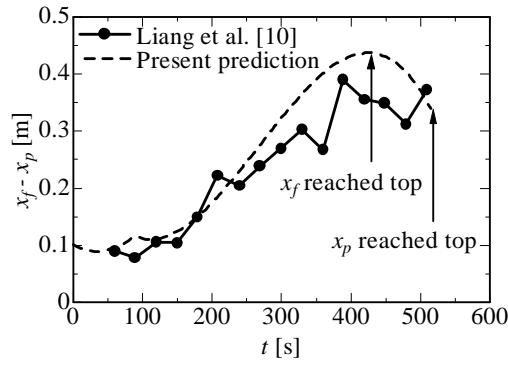
33

Fig. 20 The predicted and measured (x_f - x_p) *vs* time.

As already mentioned, Fig. 21 shows the temperature contours of the gas and solid surface (T and T_{solid}). The gas temperature is only shown on *y-x* at $z = 0$ m, T_{solid} is shown on *z-x* plane at $y = -0.0005$ m from the PMMA wall surface. Both T and T_{solid} contours gradually expand upwards from the bottom of the PMMA as the time advances. The highest T and T_{solid} are predicted to be near the bottom leading edge of the PMMA wall following Singh and Gollner's study [9]. The pyrolysis front shape ($T_{solid} = 580$ K) noticeably becomes sharp at 450 s. This tendency was also observed in the experiment of Liang et al. [10] and Tsai et al. [54] when side walls were not set. Such change is thought to be due to the corresponding change of the flame shape due to air entrainment from the sides of the PMMA wall [54]. The pyrolysis front shape becomes sharp because of the change of the flame shape, resulting in the reduction in q' and x_f. In the solid region, heat transfer in *y* and *z* directions is relatively slower than the flame spread rate. As such, most previous flame spread simulations assumed heat transfer was 1D in the solid region. However, the flame shape on the PMMA wall is not 2D as shown in Fig. 24. In Fig. 21, the predictions also captured the 2D convex shape of the temperature distribution. Hence, 1D heat transfer is assumed in the solid region but the actual flame spread phenomena is 3D and can be better captured in 3D simulations.
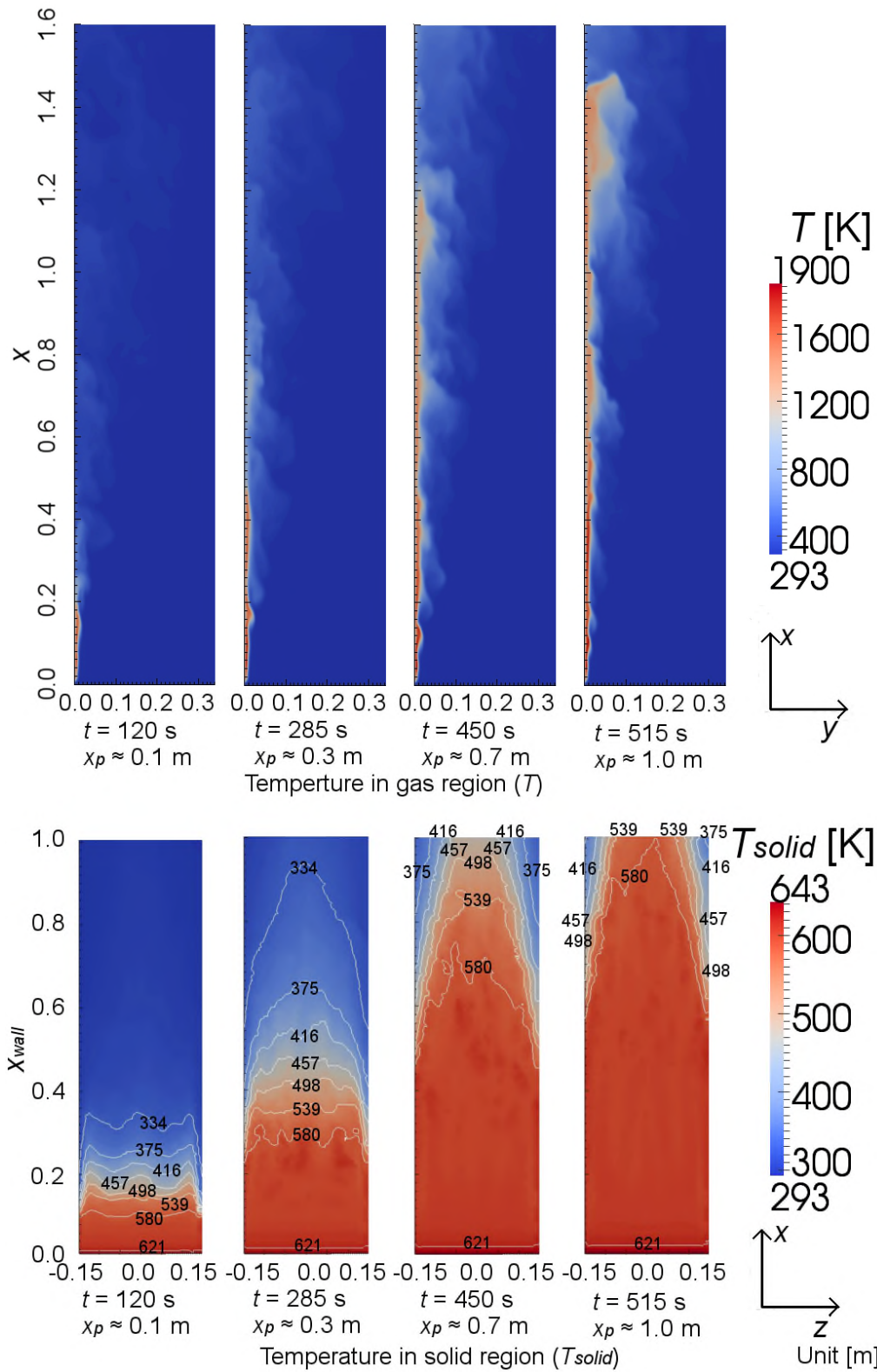
34

Fig. 21 Distribution of the gas and solid temperature. The gas temperature is for the *y-x* plane at *z* = 0 m and the solid temperature is for the *z-x* plane at *y* = -0.0005 m.

Figure 22 shows the heat release rate per width q' *vs* time. Liang et al. [10] calculated q' using $\Delta h_c = 2.42 \times 10^7$ J/kg. In the present study, q' was calculated by integrating q''' in the gas region per PMMA width; q'_2 was estimated by integrating $\Delta h_c \omega_{solid}$ in the solid region per PMMA width. Both q' and q'_2 are in reasonably good agreement with value of Liang et al. The fact that q' is very close to q'_2 indicates that the chemical reaction rate $\bar{\omega}_J$ is accurately predicted by Eqs. (5)–(7).
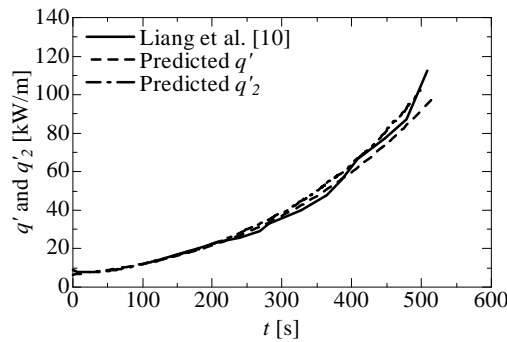

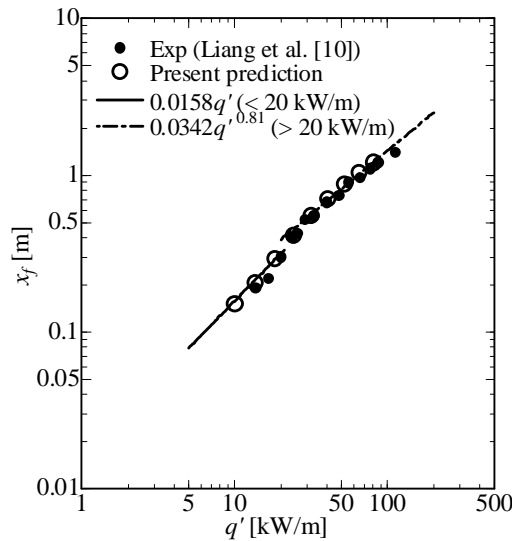Fig. 22 The heat release rate per width (q' and q'_2) *vs* time.

Fig. 23 The flame height x_f *vs* heat release rate per width q'

Figure 23 shows x_f *vs* q'. The predictions are generally in good agreement with Liang et al.'s measurements. Tsai and Draysdale [59] observed that the increase rate of x_f changed slightly from approximately 20 kW/m. This change is also captured in our results as shown in Fig. 23.
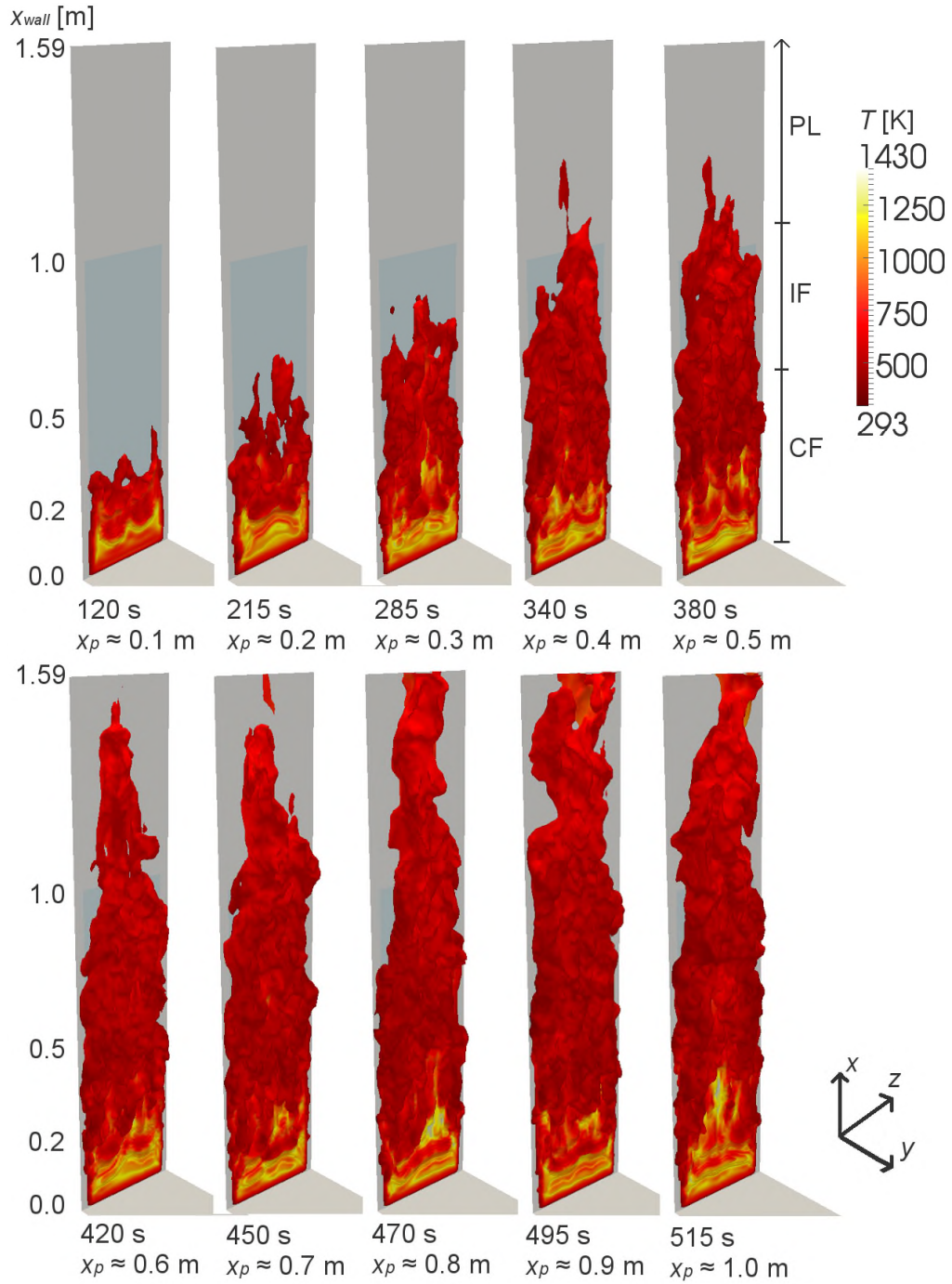
Fig. 24 The predicted iso-surfaces of the flame volume defined as the criteria $R_o = 0.99$. The continuous flame (CF), intermittent flame (IF), and plume (PL) regions are specified at 380 s.

For growth of the flame on the combustible fuel surfaces, the key parameters are the flame height and heat transfer to the unburned fuel surface. The flame height can be expressed as $x_f = K q''^n$ [4], where K and n are the fitted coefficients. Tu and Quintiere [60] estimated x_f as

$$x_f = 4.65 \left[q' / (C p_\infty T_\infty \rho_\infty g^{1/2}) \right]^{2/3}.$$ However, Tsai and Draysdale [59] found that this correlation

over-predicted x_f at $q' < 25$ kW/m, and also observed that the K and n were determined based on the configuration near the leading edge of the PMMA at $q' < 20$ kW/m. $K = 0.016$ and $n = 1.07$ were obtained when the leading edge of the PMMA was attached with the contiguous floor, which is close to Liang et al's experiment. Also, K and n is dependent on the PMMA width W at $q' > 20$ kW/m, and $K = 0.07$ and $n = 0.616$ were given with $W = 0.3$ m. In the experiment of Liang et al. [10], $K = 0.0058$ and $n = 4/3$ were obtained at $q' \leq 22$ kW/m, and $K = 0.032$ and $n = 4/5$ were given at $q' \geq 22$ kW/m. From these investigations, the threshold q' ranged approximately from 20 to 25 kW/m. The present predictions would give $K = 0.0158$ and $n = 1.0$ at $q' < 20$ kW/m; and $K = 0.0342$ and $n = 0.81$ for at $q' \geq 20$ kW/m. At $q' < 20$ kW/m, the predicted K and n are close to those obtained by Tsai and Draysdale, while the predictions are in good agreement with Liang et al's correlation at $q' \geq 20$ kW/m.
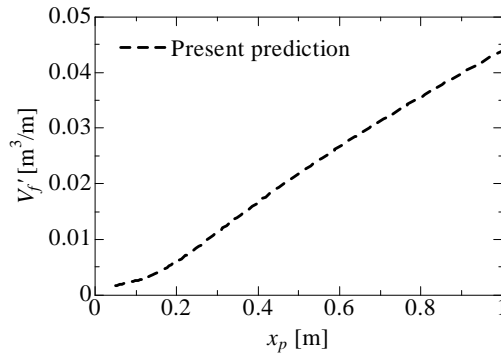

Fig. 25 The flame volume per width V'_f vs pyrolysis height x_p.

Figure 24 shows the iso-surfaces of the flame volume defined using the criteria $R_0 = 0.99$ in Eq. **(17)**. They have captured well the 3-D evolution of the flame. As can be seen in Fig. 24, the flame volume gradually expands as time passes. When $x_p \approx 0.1$ m, the flame is mostly laminar but the flame tip has started fluctuating and has likely transited to the turbulent regime. After $x_p \approx 0.3$ m, the flame tip becomes sharp and the change of the flame shape affects the change of the pyrolysis front shape as discussed earlier. Further up, strong oscillation in the z direction starts from $x_p \approx 0.7$ in the upper region ($x_{wall} > 1.0$ m). It would not be possible to capture such unsteady 3-D by 2-D RANS

38

simulations. Finally, the turbulent flame area gradually enlarges and the pyrolysis front reaches the top of the PMMA at about 515 s. However, the flame shape remains steady in the lower part at x_{wall} < 0.2 m.

Figure 25 shows the flame volume per width V'_f vs pyrolysis height x_p. The increasing rate of V'_f at 0.15 to 0.2 < x_p is relatively small at the beginning, but it increases almost linearly after that. As discussed above, it is postulated that the flame tip becomes turbulent at $x_p \approx 0.1$ and relatively strong air-entrainment happens due to turbulent mixing. Orloff et al. [4] suggested that $x_{wall} = 0.18$ m was the transition region from laminar to turbulent flow. This is thought to be the reason behind the increase rate of V'_f changed at $x_p \approx 0.15$ to 0.2 m.
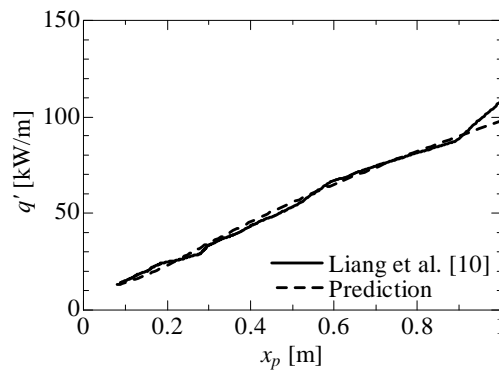

Fig. 26 The heat release rate per width q' vs pyrolysis height x_p.

Figure 26 shows the heat release rate per width q' vs pyrolysis height x_p. The predictions are in reasonably good agreement with the measurements of Liang et al. As shown in Fig. 26, at $q' = 20$ kW/m, x_p is approximately 0.15 m when the flame entered the transition region from laminar to turbulent flow. As discussed above, the increase rate of x_f changed slightly from approximately $q' = 20$ kW/m. The laminar-turbulent transition is thought to be the reason why the increase rate of x_f changed from approximately $q' = 20$ kW/m in Fig. 23.
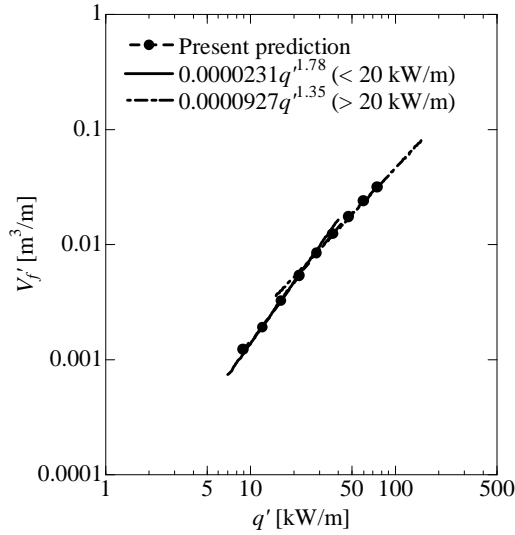
Fig. 27 The flame volume per width V'_f vs heat release rate per width q'.

Figure 27 shows the flame volume per width V'_f vs q'. V'_f vs q' is well correlated by

$V'_f = 0.0000231q'^{1.78}$ ($q' < 20$ kW/m) and $V'_f = 0.0000927q'^{1.35}$ ($q' \geq 20$ kW/m). q' can be

converted to the mass loss rate per width, and therefore the flame volume is also a function of the

mass loss rate per width. As discussed in Fig. 23, the increase rate of x_f changed slightly from

approximately 20 kW/m, and this trend is also shown here. However, it should be noted that the

exponential part of the fitted coefficient at $q' \geq 20$ kW/m is bigger than 1 (1.35), while that of x_f

was 0.81. Thus, the increasing trend of V'_f is different from that of x_f at $q' \geq 20$ kW/m.
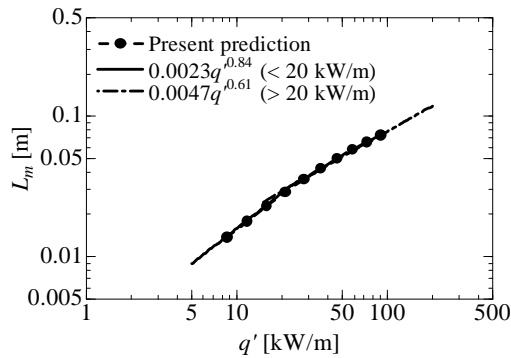

Fig. 28 The mean beam length L_m vs the heat release rate per width q'.

Figure 28 shows the predicted the mean beam length L_m *vs* q'. The predictions can be well correlated by $L_m = 0.0023q'^{0.84}$ ($q' < 20$ kW/m) and $L_m = 0.0047q'^{0.61}$ ($q' \geq 20$ kW/m). The trend of L_m also changes with q'. It should be noted that L_m is obtained using the flame volume that is calculated based on R_o. For different fuels other than PMMA, the correlation between L_m and q' should change.

Quintiere et al. [5] found through experiments that the distribution of total heat flux q_{tot} can be plotted universally against x_{wall} normalized by x_f as shown in Fig. 29. For comparison, Tsai's data is also plotted in Fig. 29. Generally, the present predictions fall between the data of Quintiere et al. and Tsai [54], while those are slightly overpredicted at $x_{wall} / x_f > 1.4$ compared with Tsai's experimental data. It is categorized as the plume region at $x_{wall} / x_f > 1.4$, and the contribution in the heating unburned fuel surface of the plume region was much smaller than in the intermittent and continuous flames [14]. Therefore, the overpredicted q_{tot} at $x_{wall} / x_f > 1.4$ is less important in this simulation.

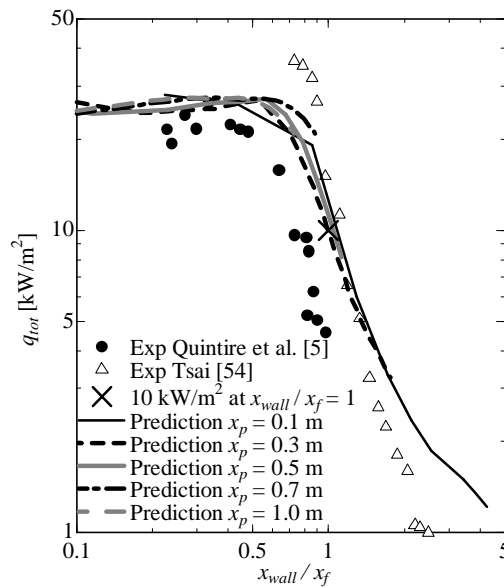Fig. 29 Total heat flux q_{tot} *vs* dimensionless height x_{wall} / x_f.

Consalvi et al. [14] commented that q_{tot} was different among different experimental reports in terms of the location of the flame tip where $x_{wall} / x_f = 1.0$. As shown in Fig. 29, $q_{tot} = 4$ kW/m^2 was in Quintiere's measurement, while $q_{tot} = 10$ kW/m^2 was in Tsai's data. This is because the different

41

definitions of the flame height used by these authors resulted in different flame tip location in their reports [55]. They correlated the heat flux in terms of $(x_{wall} - x_p) / (x_f - x_p)$, and concluded that the best correlation was obtained for 10 kW/m^2 or slightly higher value (12 kW/m^2). In this simulation, $q_{tot} = 10$ kW/m^2 are in good agreement.
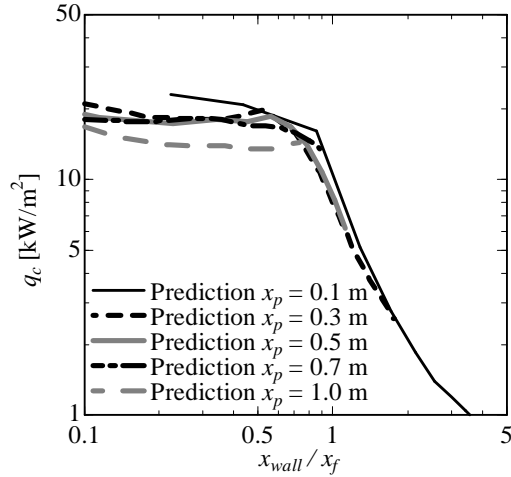
Fig. 30 Convective heat flux q_c vs dimensionless height x_{wall} / x_f.

Figure 30 shows the convective heat flux q_c vs dimensionless height x_{wall} / x_f. q_c gradually decreases when x_p increases. This is because the solid temperature at the interface $T_{solid,Inter}$ increases as the time passes. Figure 31 plots from further parametric studies of the overall radiative heat flux q_{rad} and its component due to H_2O and CO_2 and soot. The predicted q_{rad} increases when the increase of x_p as the radiative heat flux due to soot notably increases with an increase of x_p. The peak of the radiative heat flux due to soot is positioned between $0.5 < x_{wall} / x_f < 0.9$; and the peak position moves upward as x_p increases.

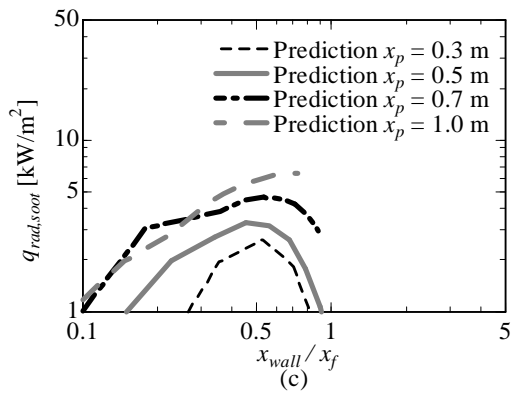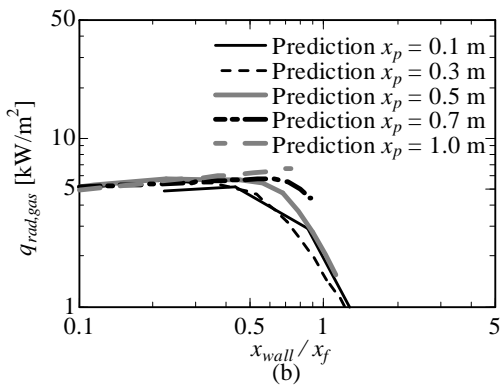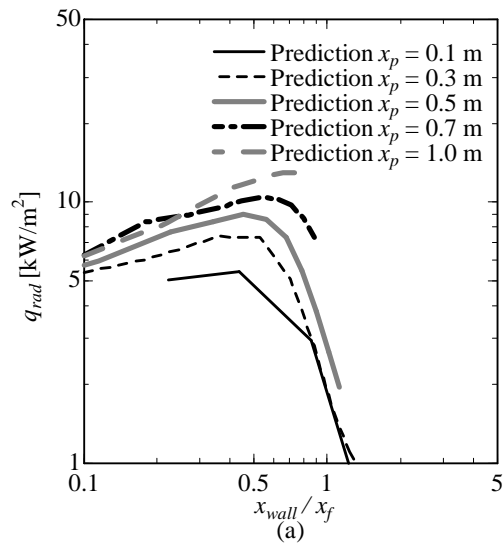Fig. 31 (a) Radiative heat flux q_{rad}; (b) $q_{rad,gas}$ radiative heat flux due to H_2O and CO_2 and (c) radiative heat flux due to soot $q_{rad,soot}$ vs dimensionless height x_{wall} / x_f.
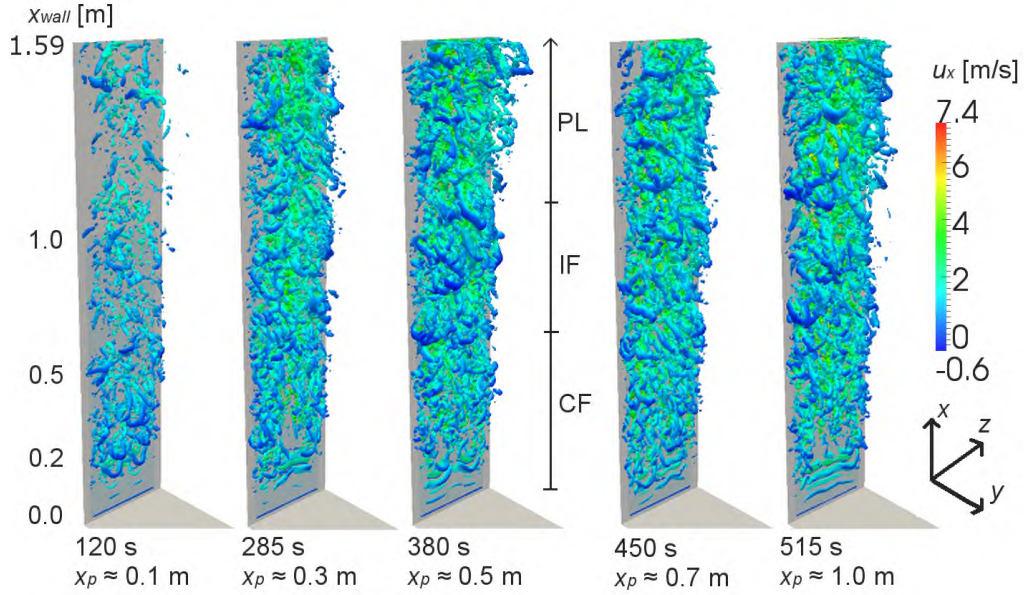
Fig. 32 The development of vortex structures illustrated by the iso-surfaces of the second invariant of gradient of the vector tensor Q = 1200. The continuous flame (CF), intermittent flame (IF), and plume (PL) regions are marked out at 380 s.

Figure 32 shows the development of the vortex structure by showing iso-surfaces of the second invariant of the gradient of the vector tensor Q = 1200. The CF, IF, and PL regions are indicated at t = 380 s. The second invariant of the gradient of the vector tensor Q is given as:

$$Q = \frac{1}{2}(\Omega_{ij}\Omega_{ij} - S_{ij}S_{ij}),$$ (34)

$$S_{ij} = \frac{1}{2}(\frac{\partial u_i}{\partial x_j} + \frac{\partial u_j}{\partial x_i}), \quad \text{and}$$ (35)

$$\Omega_{ij} = \frac{1}{2}(\frac{\partial u_i}{\partial x_j} - \frac{\partial u_j}{\partial x_i}),$$ (36)

where S_{ij} and Ω_{ij} are the symmetrical and antisymmetric parts of the velocity gradient tensor, respectively.

As shown in Fig. 32, the number of the vortex tubes are much less when $x_p \approx 0.1$ m. It gradually increases as time passes between $x_p \approx 0.1$ to 0.5 m. The number of big vortex tubes also increases with time. Finally, the pyrolysis front reached the top ($x_p \approx 1.0$) of the PMMA at about 515 s but the vortex structures remains constant at $x_{wall} < 0.2$ m between 120 to 515 s just like the flame shape in

44

Fig. 24. Generally, the relatively straight vortex tube occurs near the leading edge. Following that, the bent vortex tubes, often referred to as hairpin vortex start appearing from $x_{wall} = 0.15$ to 0.2 m. In terms of the hairpin vortex shape, the centre of the bent vortex tubes are positioned downward and both sides point to the upward direction. At $x_{wall} < 0.2$ m, the vortex structures are mostly symmetrical but they take complex vortex structures at $x_{wall} > 0.2$ m due to turbulence. Again it would not be possible to capture such dynamic evolution of the vortex tubes with 2-D RANS simulations used in most previous flame spread simulations.

Figure 33 The predicted shows the iso-surfaces of the stoichiometric mixture fraction coloured by ($\tau_{diff} - \tau_{EDC}$). Predictions carried out using $\tau_{diff} = 0.1\Delta_{filter}^2 / D$ from [19] are also plotted as reference. In Eq. (7), τ_{diff} is used in the blue region, and τ_{EDC} is used in the red region. τ_{diff} is dominant at for the laminar region $x_{wall} < 0.2$. Further upwards, the regions using τ_{EDC} increases with an increase of height. In this study, k_{sgs} is calculated based on ν_{SGS} using Eqs. (2) to (3). ν_{SGS} near the PMMA wall is reduced by the WALE model and small k_{sgs} is obtained. As a result, large τ_{EDC} was given near the wall. However, laminar-turbulent transition occurred approximately at $0.15 < x_{wall} < 0.2$ m, and τ_{EDC} becomes relatively small. The flame was affected by both the wall and turbulence, and therefore, the blue and red regions are mixed at $x_{wall} > 0.2$ m in Fig. 33. If using $\tau_{diff} = 0.1\Delta_{filter}^2 / D$ from [19], almost all regions would be assumed as laminar, the EDC model would not be activated at all. Smaller Δ_{filter} would result in this even further up along the PMMA. This has been avoided by using Eqs. (11)–(12) in the present study. In Fig. 33, the extended EDC model is used in the red region while the blue region is simulated as the laminar non-premixed flame using Eqs. (11) and (12). Predictions have also been conducted using $\tau_{diff} = 0.1\Delta_{filter}^2 / D$ from [19]

and plotted for comparison. These results show that for flame spread simulations, the use of Eq. (7) will help to ensure that the EDC is only used for the turbulent region while τ_{diff} will be used for the laminar region in line with the physics of the reactive flow.

Fig. 33 The predicted iso-surfaces of the stoichiometric mixture fraction (0.108).

Figure 34 shows the average predicted mass loss rate per unit surface area (m'/S_{Inter}) *vs* x_{wall} while Fig. 35 shows the normalized temperature and normalized upward velocity profiles *vs* normalized distance from the wall. As Liang et al. did not report on these parameters, the earlier experiments of De Ris [61] are used here for comparison based on the normalised parameters. De Ris found that the upward velocity and temperature profiles were correlated well with the soot depth d_S, which was also dependent on the mass flow rate per unit surface (m'/S_{Inter}) and x_{wall}. In the experiment [61], the side walls were set and the size of the wall with a sintered bronze burner was 1.32 m. In the simulation, the averaged results were taken between t = 550 to 580 s. The predicted mass loss rate per unit

46

surface m'/S_I *vs* x_{wall} between 550 to 580 s is shown in Fig. 34, and the averaged m'/S_I between
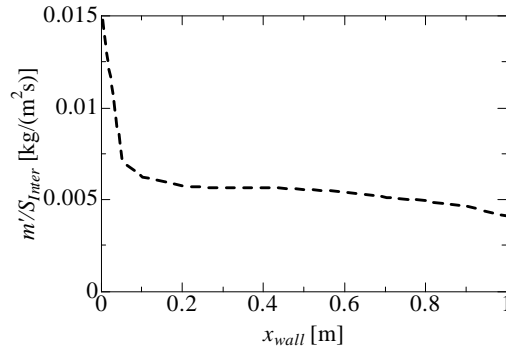
0 to x_{wall} was used to obtain d_S from [61].

Fig. 34 The average predicted mass loss rate per unit surface area
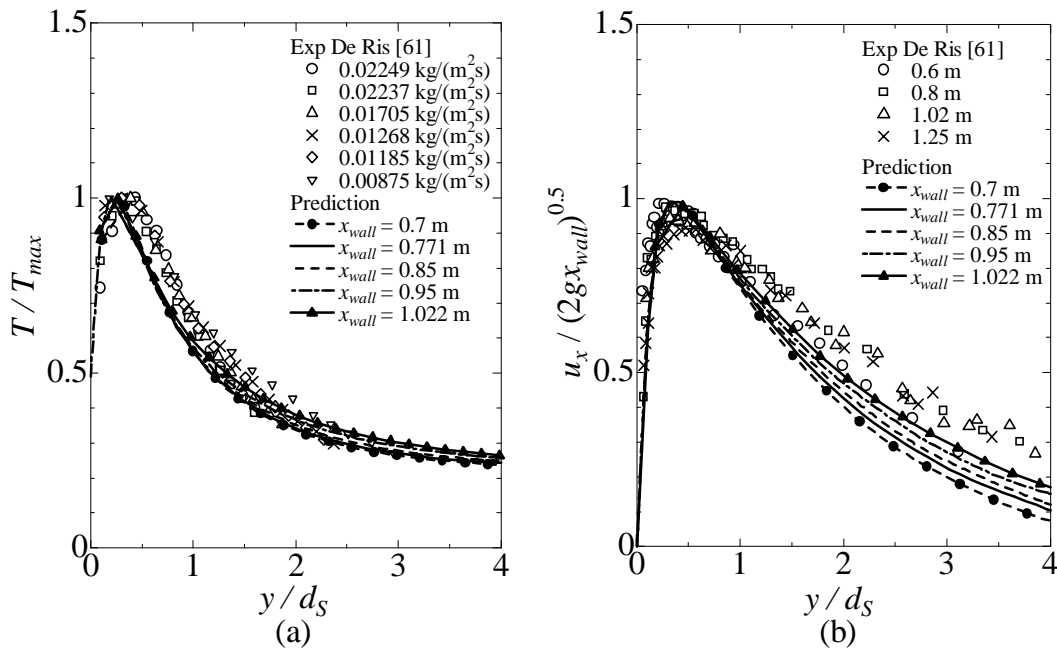(m'/S_{Inter}) *vs* $x_{wall.}$ between $t = 550$ to 580 s.

Fig. 35 The normalized mean temperature profiles (a) and normalized mean upward velocity profiles
(b) *vs* normalized distance from PMMA surface between $t = 550$ to 580 s..

As shown in Fig. 34, m'/S_{Inter} is very high at the leading edge of the PMMA because of the high

q_c as shown in Fig. 12. The lowest value is observed at $x_{wall} = 1.0$ m as the heat conduction inside the

PMMA is not still steady state. Pizzo et al. [62] suggested that combustion on the PMMA has three

stages, i.e. flame spread, transient in-depth conduction and steady stage stages. They further

suggested that m' changes from one stage to another. Hence, the simulation needs to be run for

1750–2000 s to reach steady state stage.

Figure 35 shows the normalized mean temperature profiles and mean upward velocity profiles vs normalized distance from the PMMA surface. T_{max} are 1308 K at $x_{wall} = 0.7$ m, 1294 K at $x_{wall} = 0.771$ m, 1278 K at $x_{wall} = 0.85$ m, 1259 K at $x_{wall} = 0.95$ m, 1243 K at $x_{wall} = 1.022$ m. d_s are 0.0278 m at $x_{wall} = 0.7$ m, 0.0287 m at $x_{wall} = 0.771$ m, 0.0304 m at $x_{wall} = 0.85$ m, 0.0324 m at $x_{wall} = 0.95$ m, and 0.0338 m at $x_{wall} = 1.022$ m. Here, the temperature profiles are normalized by the maximum temperature because it is dependent on the fuel. The normalized temperature profiles are in reasonably good agreement with value of De Ris. The velocity in the x direction u_x is normalized by $u_{x,\max} = (2gx_{wall})^{0.5}$ [61]. Figure 35 (b) shows the peaks of u_x are predicted well but those are slightly underestimated at $y / d_s > 1$.

In order to gain further insight of the laminar to turbulent transition, the dimensionless velocity u^+ vs dimensionless wall coordinate y^+ for different regions have been examined. As suggested by Carlsson [63], the velocity profiles near the wall involving the blowing effect can be expressed as

$$u^+ = \frac{\exp(m^+ y^+) - 1}{m^+} \qquad\qquad y^+ < 11.63, \tag{37}$$

$$u^+ = \frac{1}{\kappa_{wf}} \ln(E_{wf} y^+) + \frac{m^+}{4\kappa_{wf}^2}\left[\ln(E_{wf} y^+)\right]^2 \qquad y^+ \geq 11.63, \tag{38}$$

$$m^+ = \frac{m' / S_{Inter}}{\sqrt{\tau_w \overline{\rho}_{film}}}, \text{ and} \tag{39}$$

$$\tau_w = \overline{\rho}_{film}(\nu_{film} + \nu_{SGS,film})\frac{\partial u_x}{\partial y}, \tag{40}$$

where $\kappa_{wf} = 0.41$, $E_{wf} = 9.8$, $u^+ = u_x / u_\tau$, $y^+ = u_\tau y / \nu_{film}$, u_τ is the friction velocity [m/s], and ν_{film} is the film kinematic viscosity. The subscript "*film*" is the film value defined as $\phi_{film} = 0.5(\phi_{inter} + \phi)$, where ϕ_{inter} is the variable in the gas region at the interface. m^+ listed in Table 3 is computed from the simulation data where u_τ was obtained by solving Eqs. (37) and (38). m^+ at $y^+ < 11.63$ is computed at the cell centre at the first cell from the PMMA wall, and m^+ at $y^+ \geq 11.63$

is estimated at the coordinate where u_x is maximum.

Figure 36 shows the dimensionless velocity u^+ vs wall coordinate y^+ for different regions: (a) Laminar, (b) Transient, and (c) and (d) Fully turbulent. The predictions captured the velocity profile near the wall at both $y+ < 11.63$ and $y+ \geq 11.63$. The maximum u^+ gradually occurs at higher y^+ further up along the PMMA, i.e. at higher x_{wall}. The location for $u^+ = 1$ at the outer layer also occurs at higher y^+ with increasing x_{wall} due the growth of the boundary layer along the PMMA height. Generally, the velocity profile can be divided into several regions, $y^+ < 5$–6 is the viscous sublayer, 5–6 $< y^+ < 30$ is the buffer zone and $30 < y^+ < 500$ is the fully developed turbulent log law zone [63]. Here, the maximum u^+ is found to occur at $y+ \geq 11.63$, in the buffer zone. The value of u^+ at $y^+ = 11.63$ is assumed to be the criteria for the transition region. Using this criteria, the maximum y^+ at different height can be calculated as $y^+ \approx 12$ at $x_{wall} = 0.1$ m, $y^+ \approx 32$ at $x_{wall} = 0.3$ m, $y^+ \approx 64$ at $x_{wall} = 0.6$ m, and $y^+ \approx 139$ at $x_{wall} = 1.0$ m. Therefore, the flame is fully turbulent log law zone at $x_{wall} = 0.6$ and 1.0 m. The location $x_{wall} = 0.3$ m is the end of the buffer region to fully turbulent log law region; it is thought to be the transient region. At $x_{wall} = 0.1$ m, $y^+ \approx 12$ and close to $y^+ = 11.63$, the flame is laminar.

Table 3 m^+ at different x_{wall}

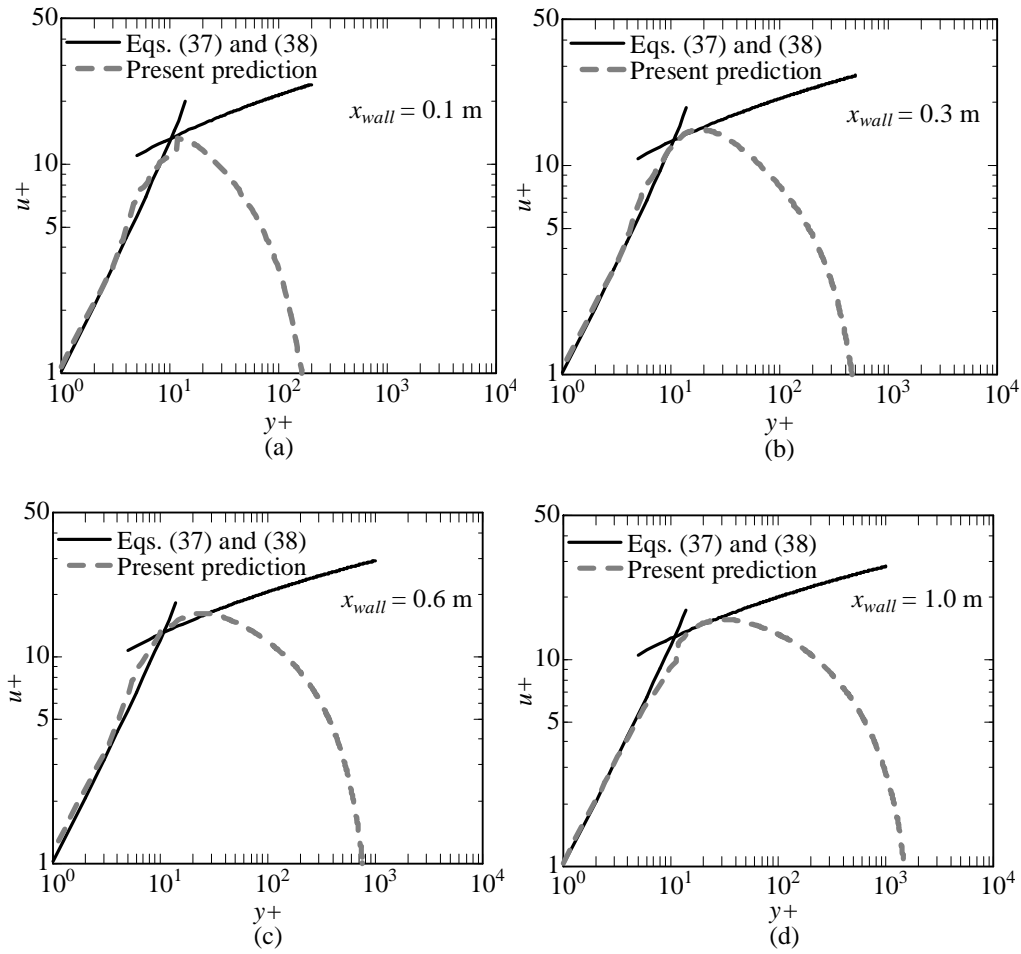| x_{wall} [m]	m^+ at $y^+ < 11.63$	m^+ at $y^+ \geq 11.63$
0.1	0.04841	0.06672
0.3	0.04037	0.05840
0.6	0.03625	0.05488
1.0	0.03064	0.04714

49

Fig. 36 The dimensionless velocity u^+ *vs* dimensionless wall coordinate y^+ for different regions: (a) Laminar region, (b) Transient, and (c) and (d) Fully turbulent between $t = 550$ to 580 s.

4　Conclusions

A fully coupled fluid-solid approach for upward flame spread has been developed within FireFOAM 2.2.x, a Large Eddy Simulation (LES) based fire simulation solver within the OpenFOAM® toolbox. The radiative heat transfer and soot treatment are fully coupled with pyrolysis calculations. Appropriate treatment has been introduced for the reaction time scale for laminar combustion and the calculation of SGS turbulent kinetic energy. The effect of in-depth radiation is treated with the relatively simple Beer's law and the solid surface regression length is calculated from the local pyrolysis rate. Systematic validation studies have been conducted with

published experimental data including simple pyrolysis tests without the gaseous region, small scale wall fires and large scale flame spread test data.

In the validation with the data of Pizzo et al. [8] which excluded gases combustion, the model captured well the length of surface regression and the time reaching the pyrolysis temperature, demonstrating that it is capable of predicting the temperature rise in flame spread condition with reasonable accuracy. For the small scale flame spread case of Huang and Gollner [52], the predicted pyrolysis height x_p and flame height x_f are locally different from the experimental data, but the measured and predicted flame spread rate v_p are in reasonably good agreement. For the wall fire of Singh and Gollner [9], the predicted convective, radiative and re-radiative heat fluxes were all in reasonably good agreement with the measurements. The inclusion of the leading edge modification was found to improve the accuracy in the convective heat flux prediction near the edge of the PMMA sample. In the validation of the soot volume fraction f_v of Hebert [58], the predicted peak amount and position are in reasonably agreement with the experimental data. In comparison with the large scale flame spread measurement of Liang et al. [10], the model predicted the pyrolysis and flame heights (x_p and x_f) with reasonably good accuracy. The predicted trends of x_p and x_f were also in line with experimental observations and measurements. The predicted flame spread rate v_p was in close agreement with the experimental data at $x_p > 0.7$ m. Overall, the predictions captured well the development of the pyrolysis front. The two stages in the development of x_f vs heat release rate per width q' were found to be divided by the threshold of 20 kW/m. The increasing trend of the flame volume per width V_f' also changed when the flame entered the transition region ($x_{wall} = 0.18$ m) from laminar to turbulent as experimentally observed by Orloff et al. [4] when q' reached 20 kW/m. Thus, the laminar to turbulent transition was thought to be the reason behind the increasing rate of x_f growth with heat release rate after q' reached 20 kW/m.

Further insights of the flame development were provided by the iso-surfaces of the flame volume. It was found that the flame shape remained steady at $x_{wall} \leq 0.2$ m even when the pyrolysis front

reached the top of the PMMA. The model captured well the heat release rate per width q' vs

pyrolysis height x_p. Two new correlations for the mean beam length L_m and V_f' vs q' were

proposed as functions of q'. Such correlations could be used to calculate the mean beam length

required as input for WSGGM radiation model. It has also been found that the increasing trend of

V_f' was different from that of x_f at $q' \geq 20$ kW/m. The predicted tendency of the total heat flux q_{tot}

was found to follow well the universal total heat flux distribution identified by Quintiere et al. [5],

and the Tsai's experimental data [54] at $x_{wall} / x_f < 1.4$, and the predicted q_{tot} at the flame tip was in

agreement with that of reported by Consalvi et al. [55]. The predicted vortex structure showed that

the hairpin vortices started appearing from $x_{wall} = 0.15$ to 0.2 m. At $x_{wall} < 0.2$ m, the vortex structures

were mostly symmetrical, but they gave the complex vortex structures at $x_{wall} > 0.2$ m. Validations

have also been carried out with the wall fire experiment of De Ris et al. [61]. The predicted

normalized temperature profile was in reasonably good agreement with the experimental data. The

predicted peaks of the normalized u_x were generally in agreement with the data but there was some

slight under-prediction at $y/d_s > 1$. It would not be possible to capture such dynamic evolution of the

flame spread phenomena with 2-D RANS simulations used in most previous flame spread

simulations.

Further parametric studies have shown the effectiveness of the present modifications to capture the

underlying physics in the flame spread phenomena. In particular, the leading edge modification was

essential for accurate calculation of the convective heat fluxes there; the proposed mean beam length

calculation has helped to ensure that the present predictions with the WSGGM better captures the

radiative heat fluxes to the PMMA surface and the proposed treatment of reaction time scale is helpful to ensure that the EDC is only used for the turbulent region while τ_{diff} will be used for the laminar region. It has also been found that while there is little change of the radiative heat flux due to H_2O and CO_2 with the increase of height, the radiative component from soot increase considerable with height, resulting in marked increase of the overall radiative heat flux q_{rad}.

The validation studies demonstrate that the present modelling approach can be used to predict upward flame spread over PMMA with reasonable accuracy. Such a fully coupled predictive tool can be used to aid fundamental studies of the flame spread phenomena such as investigating the effects of width, inclination angles and side walls on flame spread as well as the predictions of flame spread in practical applications. The new correlations developed should be of assistance to provide some estimation for the same geometrical configurations, which can be of assistance in the design of new experiments or some applications.

Given the complexity of the flame spread phenomena, it is hardly expected that a perfect comprehensive solution to the problem can be proposed. The present study has demonstrated that it is possible to obtain reasonable agreement with the measurements with the right combination of sub-models. Even if some of these sub-models might not have reached the stage of resolving all the underlying physics and reaching high accuracy, their errors compensate each other, e.g. the inaccuracy in the prediction of soot formation rate was compensated by that of soot oxidation and the inaccuracy of the convective flux at the surface is compensated by the radiative one, etc. The present study has demonstrated that this "compensation" approach in modelling complex fire phenomena can deliver reasonable predictions for practical applications.

Acknowledgments

Appendix A. Governing equations in FireFOAM used in this study.

The governing equations solved by FireFOAM is expressed as [64]:

Continuity equation

$$\frac{\partial \overline{\rho}}{\partial t} + \frac{\partial \overline{\rho}\tilde{u}_j}{\partial x_j} = 0 \tag{41}$$

Momentum equation

$$\frac{\partial \overline{\rho}\tilde{u}_j}{\partial t} + \frac{\partial \overline{\rho}\tilde{u}_i\tilde{u}_j}{\partial x_j} = \frac{\partial}{\partial x_j}\left[\overline{\rho}\left(v + v_{SGS}\right)\left(\frac{\partial \tilde{u}_i}{\partial x_j} + \frac{\partial \tilde{u}_j}{\partial x_i} - \frac{2}{3}\frac{\partial \tilde{u}_k}{\partial x_k}\delta_{ij}\right)\right] - \frac{\partial \overline{p}_{rgh}}{\partial x_i} - g_i x_i \frac{\partial \overline{\rho}}{\partial x_i} \tag{42}$$

$$\overline{p}_{rgh} = \overline{p} - \overline{\rho}g_j x_j \tag{43}$$

Mass fraction equation of gas species *J*

$$\frac{\partial \overline{\rho}\tilde{Y}_J}{\partial t} + \frac{\partial \overline{\rho}\tilde{u}_j\tilde{Y}_J}{\partial x_j} = \frac{\partial}{\partial x_j}\left[\overline{\rho}\left(D + \frac{v_{SGS}}{Sc_t}\right)\frac{\partial \tilde{Y}_J}{\partial x_j}\right] + \overline{\omega}_J + \overline{\omega}_{J,soot} \tag{44}$$

Sensible enthalpy equation

$$\frac{\partial \overline{\rho}\tilde{h}}{\partial t} + \frac{\partial \overline{\rho}\tilde{u}_j\tilde{h}}{\partial x_j} = \frac{D\overline{p}}{Dt} + \frac{\partial}{\partial x_j}\left[\overline{\rho}\left(\alpha + \frac{v_{SGS}}{Pr_t}\right)\frac{\partial \tilde{h}}{\partial x_j}\right] + q''' - \nabla \cdot q_{rad} , \tag{45}$$

where $^{-}$ and $^{\sim}$ above the variables are the time average and density weighted average, respectively. $\overline{\rho}$ is the density, t, the time, $\tilde{u}_j$, the velocity in j direction, x_j, the coordinate of j direction, v, the kinematic viscosity, v_{SGS}, the SGS kinematic viscosity, $\overline{p}_{rgh}$, the pressure excluding the gravity effect, g_i, the gravitational acceleration in i direction, $\overline{p}$, the pressure; $\tilde{Y}_J$, the mass fraction of chemical species J, D, the diffusion coefficient, Sc_t, the turbulent Schmidt number, $\overline{\omega}_J$, the reaction rate for the mass fraction equation chemical species J, $\overline{\omega}_{J,soot}$, the production (or consumption) rate due to the soot formation and oxidation of chemical species J, $\tilde{h}$, the sensible enthalpy, α, the thermal diffusivity, Pr_t, the turbulent Prandtl number, q''', the heat release rate per volume due to the chemical reaction, and q_{rad} is the radiative heat flux. v is calculated based on

Sutherland's law [18,65], and α is obtained by $\alpha = \lambda / (Cp\bar{\rho})$, where λ is the thermal conductivity obtained by the modified eucken correction [65], and the specific heat at constant pressure Cp is calculated by [18, 65]. D is given as $D = \alpha$.

Appendix B. The extended eddy dissipation concept for combustion

The eddy dissipation model was originally proposed by Magnussen et al. [66]. The eddy dissipation model was extended to the eddy dissipation concept (EDC) model by giving the consideration of turbulence structures by Magnussen [67], and the models have since been widely applied to combustion simulations [68,69]. However, the original formulas were strongly dependent on grid resolutions [70], which was thought to be caused by the direct replacement of the total kinetic energy with the SGS kinetic energy [24]. In order to overcome this problem, Chen et al. [26] modified the EDC formulations following the energy cascade concept [71] and extended it to LES.

In Fig. 37, u_n, L_n, S_n and $q_{therm,n}$ are the velocity scale [m/s], length scale [m], strain rate [1/s], and the thermal energy conversion rate [m^2/s^3] resulting from the dissipation, and subscript n is the n-th structure level, and w_n [m^2/s^3] is the sum of the mechanical energy feed rate on all subsequent levels.

In the energy cascade concept [71], w_n, $q_{therm,n}$ and S_n are modeled as

$$w_n = \frac{3}{2}C_{D1}S_n u_n^2 , \tag{46}$$

$$q_{therm,n} = C_{D2}\nu S_n^2 , \text{ and} \tag{47}$$

$$S_n = \frac{u_n}{L_n} , \tag{48}$$

where C_{D1} and C_{D2} are the model constants. Ertesvåg and Magnussen [71] modeled S_n related to adjacent structure levels as

$$S_n = 2S_{n-1} . \tag{49}$$

According to Eq. (47) and (49), $q_{therm,n}$ is given as

$$q_{therm,n} = 4q_{therm,n-1}.$$ (50)

The total dissipation rate of the kinetic energy ε [m²/s³] is modeled as [71]

$$\varepsilon = q'_{therm} + q''_{therm} \cdots + q_{therm,n} \cdots + q_{therm,SGS} + q_{therm,SGS+1} \cdots q^*_{therm}.$$ (51)

Substituting Eq. (50) into Eq. (51), and then applying the series theory.

$$4q^*_{therm} - q'_{therm} = 3\varepsilon.$$ (52)

Similarly, w_{SGS} on the filter size "Δ_{filter}" level is given as

$$w_{SGS} = q_{therm,SGS} + q_{therm,SGS+1} + q_{therm,SGS+2} \cdots + q^*_{therm}.$$ (53)

By substituting Eq. (50) into Eq. (53), Eq. (53) becomes

$$4q^*_{therm} - q_{therm,SGS} = 3w_{SGS}.$$ (54)

Then, by subtracting Eq. (54) from (52), the following equation is given as

$$\varepsilon = w_{SGS} + \frac{1}{3}q_{therm,SGS} - \frac{1}{3}q'_{therm}.$$ (55)

Chen et al. [25] considered that q'_{therm} is negligible because the energy dissipation into heat mainly occurs on the small scale. Using Eq. (46) and (47), the Eq.(55) is given as

$$\varepsilon \approx w_{SGS} + \frac{1}{3}q_{therm,SGS} = \frac{3}{2}C_{D1}\frac{u^3_{SGS}}{\Delta_{filter}} + \frac{1}{3}C_{D2}\nu\frac{u^2_{SGS}}{\Delta^2_{filter}}.$$ (56)

u_{SGS} is estimated by $\sqrt{2/3k_{SGS}}$, where k_{SGS} is the SGS turbulent kinetic energy [m²/s²], and therefore Eq. (56) becomes

$$\varepsilon \approx \sqrt{\frac{2}{3}}C_{D1}\frac{k_{SGS}^{3/2}}{\Delta_{filter}} + \frac{2}{9}C_{D2}\nu\frac{k_{SGS}}{\Delta^2_{filter}}.$$ (57)

Because of the energy conservation and Eqs. (46) and (48), ε is rewritten as

$$\varepsilon = w' = \frac{3}{2}C_{D1}\frac{u'^3}{L'},$$ (58)

where L' is the integral length scale. u' is estimated by $\sqrt{2/3k}$, where k is the total kinetic energy [m²/s²]. Therefore k is given as

$$k = \left(\frac{3}{2C_{D1}{}^2}\right)^{1/3}(\varepsilon L')^{2/3},\qquad(59)$$

where Chen et al. [26] used the characteristics length of fire plumes for L' [72] for the simulations of free standing pool fires given as

$$L' = \left(\frac{q}{\rho_\infty Cp_\infty T_\infty g^{1/2}}\right)^{2/5},\qquad(60)$$

where q is the heat release rate, ρ_∞ the ambient density, Cp_∞ the ambient specific heat at constant pressure, g the gravitational acceleration, and T_∞ the ambient temperature. For the last structure level, w^* is expected to be equal to q^* in terms of the energy conservation. Using (46)–(47) and (52), the L^* and u^* can be given as

$$L^* = \frac{2}{3}\left(\frac{3C_{D2}{}^3}{C_{D1}{}^2}\right)^{1/4}\left(\frac{v^3}{\varepsilon}\right)^{1/4},\text{ and}\qquad(61)$$

$$u^* = \left(\frac{C_{D2}}{3C_{D1}{}^2}\right)^{1/4}(v\varepsilon)^{1/4},\qquad(62)$$

where Chen et al. [26] assumed that the Kolmogorov length is equal to the characteristics length of the fine structures, and $C_{D1} = 0.5$ and $C_{D2} = 0.75$ are analytically derived with this assumption. The time averaged reaction rate of fuel $\overline{\omega}_{fu,EDC}$ is calculated as

$$\overline{\omega}_{fu,EDC} = \overline{\rho}\dot{m}^*\frac{\gamma\chi}{1-\gamma\chi}\min(\tilde{Y}_{fu},\frac{\tilde{Y}_{O_2}}{s})\qquad\text{kg/s/m}^3,\qquad(63)$$

where $\dot{m}^*$ is the mass transfer rate between the fine (last) structures and surrounding fluids, γ, mass fraction of the fine structures, χ, and reacting fraction of the fine structures, and s is the stoichiometric O_2-to-fuel mass ratio. Wang et al. [24] further proposed that χ is given as:

$$\chi = \begin{cases} \dfrac{\tilde{Z}}{Z_{st}} & 0 \le \tilde{Z} < Z_{st} \\[2ex] \dfrac{1-\tilde{Z}}{1-Z_{st}} & Z_{st} \le \tilde{Z} \le 1 \end{cases},\qquad(64)$$

where $\tilde{Z}$ is the density weighted mixture fraction, and Z_{st} is the stoichiometric mixture fraction. $\tilde{Z}$ is calculated by Bilger's definition [73] as

$$\tilde{Z} = \frac{2\tilde{Y}_C / M_C + 0.5\tilde{Y}_H / M_H + (Y_{O,\infty} - \tilde{Y}_O) / M_O}{2Y_{C,inlet} / M_C + 0.5Y_{H,inlet} / M_H + Y_{O,\infty} / M_O} , \text{ and} \tag{65}$$

$$Z_{st} = \frac{Z_{O,\infty} / M_O}{2Y_{C,inlet} / M_C + 0.5Y_{H,inlet} / M_H + Y_{O,\infty} / M_O} , \tag{66}$$

where $\tilde{Y}_C$, $\tilde{Y}_H$, and $\tilde{Y}_O$ are the density weighted elemental mass fractions for the elements carbon, hydrogen and oxygen, M_C, M_H, and M_O are the atomic masses for the elements carbon, hydrogen and oxygen, and the subscript "inlet" and "∞" are the inlet and ambient.

$\dot{m}^*$ can be calculated from the characteristic velocity and length scale of the fine structures expressed as [25]:

$$\dot{m}^* = \frac{2u^*}{L^*} = \left(\frac{3}{C_{D2}}\right)^{1/2} \left(\frac{\varepsilon}{\nu}\right)^{1/2} \quad s^{-1}. \tag{67}$$

γ is obtained by [25,26]

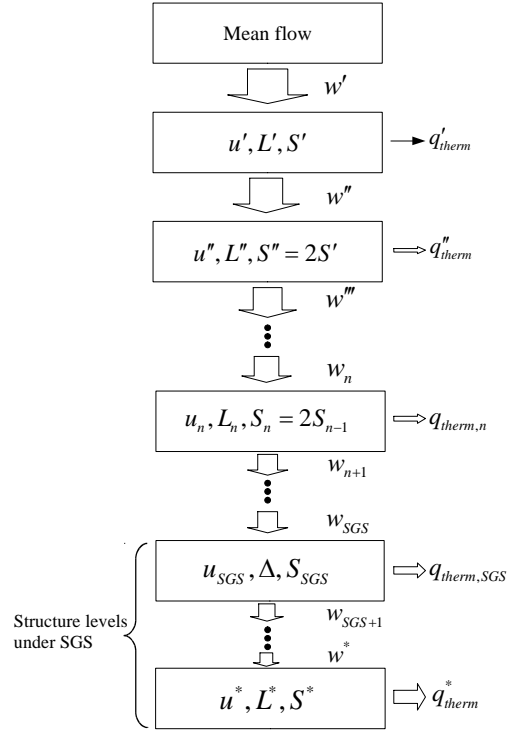$$\gamma = \left(\frac{L^*}{L'}\right)^{0.2}. \tag{68}$$

Fig. 37 The turbulent energy cascade in the
LES framework suggested by Chen et al. [25,26].

Appendix C. Soot formation and oxidation models

The soot model is adopted from the development of Chen et al. [25] based on PaSR approach [74]. In the following, the mass balance in the soot model is explained. The reader is recommended to refer to Chen et al. [25] for further details of the model. In this model, the soot formation is simplified as

$$C_x H_y O_{z,(g)} \rightarrow C_x H_y O_{z,(S)} ,$$ (69)

where subscript $C_x H_y O_{z,(g)}$ is the gas phase fuel and $C_x H_y O_{z,(S)}$ is the soot particle formed from $C_x H_y O_{z,(g)}$.

The mass fraction equation of soot is given as:

$$\frac{\partial \overline{\rho} \tilde{Y}_S}{\partial t} + \frac{\partial \overline{\rho} \tilde{u}_j \tilde{Y}_S}{\partial x_j} = \frac{\partial}{\partial x_j}\left[\overline{\rho}\left(D_S + \frac{\nu_{SGS}}{Sc_t} \right) \frac{\partial \tilde{Y}_S}{\partial x_j} \right] + \overline{\omega}_S , \text{ and}$$ (70)

$$\bar{\omega}_S = \bar{\omega}_{S,f} - \bar{\omega}_{S,ox} \qquad \text{kg/s/m}^3, \tag{71}$$

where $\tilde{Y}_S$ is the mass fraction of soot, $\bar{\omega}_S$, the total soot formation rate, $D_S = 0.01D$ following [25], $\bar{\omega}_{S,f}$, the time averaged soot formation rate, and $\bar{\omega}_{S,ox}$ is the time averaged soot oxidation rate. $\bar{\omega}_{S,f}$ in Eq. (71) is given by

$$\bar{\omega}_{S,f} = \frac{\tau_{S,C}}{\tau_{S,C} + \tau_{mix}} \omega_{S,f} \qquad \text{kg/s/m}^3, \tag{72}$$

where subscript f and ox mean formation and oxidation, respectively. $\tau_{S,C}$ is the chemical time scale of the soot formation, τ_{mix} is the turbulent mixing time scale [25], and $\omega_{S,f}$ is the soot formation rate. Chen et al. [25] estimated τ_{mix} from the geometrical mean of the time scale, i.e., integral time scale τ_{integ} and the smallest time scale, i.e., Kolmogorov time scale τ_η, and given as

$$\tau_{mix} = \sqrt{\tau_\eta \tau_{integ}} = \sqrt{\left(\frac{\nu}{\varepsilon}\right)^{0.5} \left(\frac{k}{\varepsilon}\right)} \qquad \text{s}, \tag{73}$$

Chen et al. estimated $\tau_{S,C}$ as $\tau_{S,C} = C_{sp}L_{sp}$, where C_{sp} and L_{sp} are the fixed model constant that is independent of fuel type [25] and L_{sp} is the smoke point height. $C_{sp} = 0.364$ m/s is estimated based on the laminar ethylene diffusion flame, while $\tau_{S,C}$ is computed based on the PaSR approach [74] following Wang et al. [75]:

$$\tau_{S,C} = \frac{\bar{\rho}\tilde{Y}_S}{\omega_{S,f}} \qquad \text{s, and} \tag{74}$$

$$\omega_{S,f} = \begin{cases} \dfrac{4.4 \times 10^{-6}}{L_{sp}} \tilde{\rho}^2 Y_{fu,inlet} \dfrac{\tilde{Z} - Z_{st}}{1 - Z_{st}} \tilde{T}^{2.25} \exp(-\dfrac{2000}{\tilde{T}}) & Z_{ox} \le \tilde{Z} \le Z_f \\ 0 & \text{else} \end{cases} \qquad \text{kg/s/m}^3, \tag{75}$$

where $Z_{ox} = Z_{st}$ [76], $Z_f = 2.5Z_{st}$ [76], $Y_{fu,inlet}$ is the mass fraction of sooty fuel at the inlet, and $\tilde{T}$ is the density weighted temperature. L_{sp} of CH_4 and $C_5H_8O_2$ are set to 0.29 and 0.105 following [40].

In Chen et al.'s soot oxidation model, the soot oxidation reaction is considered as

$$C_xH_yO_{z,(S)} + (x + \frac{y}{4} - z)O_2 = xCO_2 + \frac{y}{2}H_2O\text{-}\Delta h_{c,S} \,, \tag{76}$$
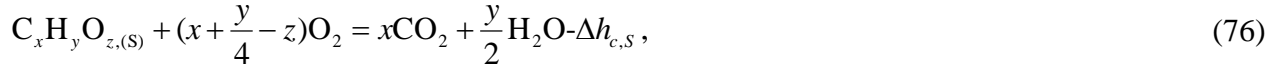
where $\Delta h_{c,S}$ is the heat of combustion of the soot particle. $\Delta h_{c,S}$ is evaluated as $\Delta h_{c,S} = \Delta h_c$, where Δh_c is the heat of combustion of $C_xH_yO_{z,(g)}$.

Chen et al.'s soot model used the EDC model to obtain the time averaged soot oxidation rate $\bar{\omega}_{S,ox}$ as:

$$\bar{\omega}_{S,ox} = \begin{cases} \bar{\rho}\tilde{Y}_S \dot{m}^* \dfrac{\gamma\chi}{1-\gamma\chi} & 0 \leq Z \leq Z_{ox} \text{ and } T \geq 1300 \, K \\ 0 & \text{else} \end{cases} \quad \text{kg/s/m}^3. \tag{77}$$

$\bar{\omega}_{J,soot}$ in Eq. (44) is computed from $\bar{\omega}_{S,f}$ and $\bar{\omega}_{S,ox}$.

In terms of fuel species, $\bar{\omega}_{J,soot}$ is given as

$$\bar{\omega}_{J,soot} = -\bar{\omega}_{S,f} \quad \text{kg/s/m}^3, \tag{78}$$

where $J = C_5H_8O_2$ or CH_4 in this study. Also, $\bar{\omega}_{O_2,soot}$, $\bar{\omega}_{CO_2,soot}$, and $\bar{\omega}_{H_2O,soot}$ are obtained following the mass balance in Eq. (44) from [25] given as

$$\bar{\omega}_{J,soot} = (v''_J - v'_J)\frac{M_J}{M_{fu}}\bar{\omega}_{S,ox} \quad \text{kg/s/m}^3, \tag{79}$$

where $J = O_2$, CO_2, or H_2O.

References

1   D. Drysdale, A. J. R. Macmillan, Fire Safety Journal 18 (3) (1992) 245–254.

2   A. C. Fernandez-Pello, Combust. Flame 31 (1978) 135–148.

3   M. Chaos, M. M. Khan, N. Krishnamoorthy, J. L. De Ris, S. B. Dorofeev, Proc. Combust. Inst. 33 (2) (2011) 2599–2606.

4   L. Orloff, J. De Ris, G. H. Markstein, Proc. Combust. Inst. 15 (1) (1975) 183–192.

5   J. Quintiere, M. Harkleroad, Y. Hasemi, Combustion Science and Technology 48 (3–4) (1986) 191–222.

6 K. Saito, J. G. Quintiere, F. A. Williams, Proc. 1st Int. Symp. (1986) 75–86.

7 I. T. Leventon, S. I. Stoliarov, Proc. Combust. Inst. 34 (2) (2013) 2523–2530.

8 Y. Pizzo, C. Lallemand, A. Kacem, A. Kaiss, J. Gerardin, A. Acem, P. Boulet, B. Porterie, Combust. Flame 162 (1) (2015) 226–236.

9 A. V. Singh, M. J. Gollner, Combust. Flame 162 (5) (2015) 2214–2230.

10 C. Liang, X. Cheng, H. Yang, H. Zhang, K. K. Yuen, Fire and Materials (2015) doi: 10.1002/fam.2304.

11 I. T. Leventon, J. Li, S. I. Stoliarov, Combustion and Flame 162 (10) (2015) 3884–3895.

12 A. Kacem, Y. Pizzo, G. Boyer, S. Suard, B. Porterie, Comparative Evaluation of Clear PMMA Pysolysis Models, 9th Mediterranean Combustion Symposium, June 7–11, 2015, Greece.

13 J. Gong, X. Zhou, J. Li, L. Yang, International Journal of Heat and Mass Transfer (91) (2015) 225–234.

14 J. L. Consalvi, Y. Pizzo, B. Porterie, Fire Safety Journal 43 (5) (2008) 351–362.

15 J. W. Kwon, A. D. Nicholas, W. L. Christopher, Fire technology 43 (4) (2007) 255–284.

16 N. Ren, Y. Wang, A. Trouve, Procedia Engineering, 62 (2013) 443–452.

17 FM Global, FireFOAM 2.2.x, Available from: https://github.com/fireFoam-dev/fireFoam-2.2.x

18 OpenFOAM Ltd., OpenFOAM, Source code and documentations are available from: http://www.openfoam.com/

19 N. Ren, Y. Wang, S. Vilfayeau, A. Trouvé, Combustion and Flame 169 (2016) 194–208.

20 P. Sagaut, Large Eddy Simulation for Incompressible Flows: An Introduction Third Edition, Springer-Verlag Berlin Heidelberg New York, 1998

21 S. Yuan, Z. Jian, Fire safety journal 44 (3) (2009) 349–362.

22 W. Xie, P. E. Desjardin, Combustion and Flame 156 (2009) 522–530.

23 J. L. Consalvi, B. Porterie, M. Coutin, L. Audouin, C. Casselman, A. Rangwala, S. G. Buckley, J. L. Torero, Fire Safety Science 8 (2005) 397–408.

24 C. J. Wang, J. Wen, Z. B. Chen, S. Dembele, International Journal of Hydrogen Energy 39 (35)

(2014) 20560–20569.

25 Z. Chen, J. Wen, B. Xu, S. Dembele, Fire Safety Journal 64 (2014) 12–26.

26 Z. Chen, J. Wen, B. Xu, S. Dembele, Int. J Heat and Mass Transfer 70 (2014) 389–408.

27 I. Sikic, J. Wen and S. Dembele, Evaluation of Different Schemes of the Weighted-Sum-of-Grey-Gases Model for Fire Simulations, 9th U. S. National Combustion Meeting May 17-20, 2015, Cincinnati, Ohio, USA.

28 J. Wen and K. Fukumoto, Large Eddy Simulation of Upward Flame Spread on PMMA wall, 9th U. S. National Combustion Meeting May 17–20 2015, Cincinnati, Ohio.

29 J. H. Ferziger, M. Peric. Computational Methods for Fluid Dynamics, Springer-Verlag Berlin Heidelberg New York, Germany, 1999.

30 F. Nicoud, D. Ducros, Flow, Turbulence and Combustion 62 (3) (1999) 183–200.

31 O. Colin, F. Ducros, D. Veynante, T. Poinsot, Physics of Fluids 12 (7) (2000) 1843–1863.

32 A. C. Fernandez-Pello, Combustion Science and Technology 17 (3–4) (1977) 87–98.

33 J. Warnatz, U. Maas, R.W. Dibble, Combustion 4th edition, Springer, Berlin , Germany, 2006, p. 321.

34 L. Vervisch, T. Poinsot, Annual Review of Fluid Mechanics 30 (1) (1998) 655–691.

35 P. Norbert, Turbulent Combustion, Cambridge University Press, Cambridge, United Kingdom, 2004, p. 31.

36 T. F. Smith, Z. F. Shen, J. N. Frledman, Journal of Heat Transfer 104 (4) (1982) 602‑608.

37 C. Lautenberger, J. L. de Ris, N. A. Dembsey, J. R. Barnett, H. R. Baum, Fire Safety Journal 40 (2) (2005) 141‑176.

38 L. Orloff, A. T. Modak, R. L. Alpert, Symposium (International) on Combustion 16 (1) (1977).

39 W. Yang, B. Wlodzimierz, Numerical study of fuel temperature influence on single gas jet combustion in highly preheated and oxygen deficient air, Energy 30 (2) (2005) 385‑398.

40 A. Tewarson, Prediction of fire properties of materials. part 1: aliphatic and aromatic

hydrocarbons and related polymers, Report NBS-GCR-86-521, National Institute of Standards and Technology, Gaithersburg, MD, 1986.

41 A. Kacem, Y. Pizzo, G. Boyer, S. Suard, B. Porterie, Comparative Evaluation of Clear PMMA Pysolysis Models, 9th Mediterranean Combustion Symposium, June 7–11 2015, Greece.

42 J. E. J. Staggs, Fire safety journal 39 (8) (2004) 711‑720.

43 J. P. de Wilde, The Heat of Gasification of Polyethylene and Polymethylmethacrylate, Memorandum M-593, Report PML 1988 C42, SFCC Publication No. 53, Delft University of Technology, 1988.

44 F. Jiang, J. L. De Ris, M. M. Khan, Fire Safety Journal 44 (1) (2009) 106–112.

45 J. Staggs, Combustion and Flame 161 (12) (2014) 3229–3236.

46 Y. Sohn, S. W. Baek, T. Kashiwagi, Combust. Sci. Tech. 145 (1999) 83‑108.

47 Altuglas International, General information and physical properties, available from: http://www.plexiglas.com/

48 P. Boulet, J. Gérardin, Z. Acem, G. Parent, A. Collin, Y. Pizzo, B. Porterie, International Journal of Thermal Sciences 82 (2014) 1‑8.

49 J. P. Holman, Heat Transfer 10th edition, McGraw-Hill, U.S., 2008, p. 346.

50 K. Fukumoto, Y. Ogami, Heat Transfer‒Asian Research 39 (5) (2010) 292–313.

51 D. A. Delichatsios, Combustion Science and Technology 39 (1–6) (1984), 195–214.

52 X. Huang, M. J. Gollner, Correlations for evaluation of flame spread over an inclined fuel surface, Fire safety science-proceedings of the eleventh international symposium (2014) 222–233.

53 M. Muñoz, J. Arnaldos, J. Casal, E. Planas, Combustion and Flame 139 (3) (2004) 263–277.

54 K. C. Tsai, Fire Safety Journal 46 (5) (2011) 294‑304.

55 J. L. Consalvi, Y.　Pizzo, B. Porterie, J.L. Torero, Fire safety journal 42 (5) (2007) 384‑392.

56 Y. Pizzo, J. L. Consalvi, P. Querre, M. Coutin, B. Porterie, Fire safety journal 44 (2009) 407‑

414.

57 W. L. Grosshandler, RADCAL: A Narrow-band Model for Radiation Calculations in Combustion Environment, NIST Technical Note 1402, National Institute of Standards and Technology, Gaithersburg, MD, USA, 1993.

58 D. Hebert, A. Coppalle, M. Talbaut, Proc. Combust. Inst. 34 (2) (2013), 2575–2582.

59 K. C. Tsai, D. Drysdale, Fire and materials 26 (6) (2002) 279–287.

60 K. M. Tu, J. G. Quintiere, Fire technology 27 (3) (1991) 195–203.

61 J. L. De Ris, G. H. Markstein, L. Orloff, P. A. Beaulieu, Fire Safety Science 7 (2003) 259–270.

62 Y. Pizzo, J. L. Consalvi, P. Querre, M. Coutin, L. Audouin, B. Porterie, J. L. Terero, Combustion and Flame 152 (3) 2008 451–460.

63 J. Carlsson, Computational strategies in flame-spread modelling involving wooden surfaces -An evaluation study, Report 1028 Lund 2003, Lund University, Sweden.

64 Y. Wang, P. Chatterjee, J. L. de Ris, Proceedings of the Combustion Institute, 33(2): 2473-2480 (2011).

65 W. S. Hinman, C. T. Johansen, Shock Waves 26 (2015) 1–11.

66 B. F. Magnussen, B. H. Hjertager, Symposium (International) on Combustion 16 (1) (1977)

67 B. F. Magnussen, B. W. Hjertager, On the Structure of Turbulence and a Generalized Eddy Dissipation Concept for Chemical Reaction in Turbulent Flow, 19th AIAA Aerospace Meeting, St. Louis, USA, 1981.

68 I. R. Gran, B. F. Magnussen, Combustion Science and Technology 119 (1–6) (1996) 191–217

69 A. Habibi, B. Merci, G. J. Heynderickx, AIChE journal 53 (9) (2007) 2384–2398.

70 C. Fureby, C. Löfström, Symposium (International) on Combustion 25 (1) (1994) 1257‑1264.

71 I. S. Ertesvåg, B. F. Magnussen, Combustion Science and Technology 159 (1) (2000) 213–235.

72 H. R. Baum, K. B. McGrattan, R. G. Rehm, Journal of the Heat Transfer Society of Japan 35 (139) (1997) 45–52.

73 R. W. Bilger, S. H. Stårner, R. J. Kee, Combustion and Flame 80(2) (1991) 135–149.

74 V. Golovitchev, J. Chomiak, Numerical Modelling of High-Temperature Air Flameless Combustion, Proceeding of the 6th European Conference INFUB, Lisbon, Portugal, Vol. 1, 2002.

75 C. J. Wang and J. X. Wen, EDC and PaSR based Soot Models in FireFOAM, FM Global, 6th FM Global Open Source CFD Fire Modelling Workshop May 15–16 2014, MA, USA.

76 T. Beji, J. P. Zhang, W. Yao, M. Delichatsios, A novel soot model for fires: validation in a laminar non-premixed flame, Combustion and Flame 158 (2) (2011) 281–290.

List of Figures

Fig. 13 Sensitivity test for radiation sub models

Fig. 14 Sensitivity test for the reaction time scale expressions.

Fig. 15 The measured (Exp) and predicted convective heat fluxes q_c vs dimensionless height x_{wall}/H depending on using Eq. (31) and Courant number (C_r).

Fig. 16 The predicted mean soot volume fraction (f_v) and temperature profiles vs distance from the PMMA wall y at (a) $x_{wall} = 0.255$ and (b) $x_{wall} = 0.335$ m.

Fig. 17 The predicted and measured pyrolysis (x_p) flame (x_f) heights vs time

Fig. 18 The flame spread rate v_p vs pyrolysis height x_p.

Fig. 19 The predicted and measured flame height x_f vs pyrolysis height x_p.

Fig. 20 The predicted and measured the (x_f - x_p) vs time.

Fig. 21 Distribution of the gas and solid temperature. The gas temperature is y-x plane at $z = 0$ m, and the solid temperature is z-x plane at $y = -0.0005$ m.

Fig. 22 The heat release rate per width (q' and q'_2) vs time.

Fig. 23 The flame height x_f vs heat release rate per width q'

Fig. 24 The predicted iso-surfaces of the flame volume defined as the criteria $R_o = 0.99$. The continuous flame (CF), intermittent flame (IF), and plume (PL) regions are specified at 380 s.

Fig. 25 The flame volume per width V'_f vs pyrolysis height x_p.

Fig. 26 The heat release rate per width q' vs pyrolysis height x_p.

Fig. 27 The flame volume per width V'_f vs heat release rate per width q'.

Fig. 28 The mean beam length L_m vs the heat release rate per width q'.

Fig. 29 Total heat flux q_{tot} vs dimensionless height x_{wall}/x_f.

Fig. 30 Convective heat flux q_c vs dimensionless height x_{wall}/x_f.

Fig. 31 (a) Radiative heat flux q_{rad}, (b) radiative heat flux due to H_2O and CO_2, and (c) radiative heat flux due to soot vs dimensionless height x_{wall}/x_f.

Fig. 32 The development of vortex structures by showing iso-surfaces of the second invariant of

gradient of the vector tensor $Q = 1200$. The continuous flame (CF), intermittent flame (IF), and plume (PL) regions are depicted at 380 s.

Fig. 33 The predicted iso-surfaces of the stoichiometric mixture fraction (0.108).

Fig. 34 The average predicted mass loss rate per unit surface area (m' / S_{Inter}) vs $x_{wall.}$ between $t =$ 550 to 580 s.

Fig. 35 The normalized mean temperature profiles (a) and normalized mean upward velocity profiles (b) vs normalized distance from PMMA surface between $t = 550$ to 580 s.

Fig. 36 The dimensionless velocity u^+ vs dimensionless wall coordinate y^+ for different regions: (a) Laminar region, (b) Transient, and (c) and (d) Fully turbulent between $t = 550$ to 580 s.

Fig. 37 The turbulent energy cascade in the LES framework suggested by Chen et al. [25,26].

List of Tables

Table. 1 The gas phase model input parameters.
Table. 2 The pyrolysis model parameters
Table. 3 m^+ at different x_{wall}.